

Modeling Nonlinear Optical Response in 2D materials from Nonequilibrium Quantum Dynamics

WENWEN MAO

(Universität Hamburg)

**DISSERTATION ZUR
ERLANGUNG DES DOKTORGRADES
AN DER FAKULTÄT FÜR MATHEMATIK, INFORMATIK UND
NATURWISSENSCHAFTEN, FACHBEREICH PHYSIK,
DER UNIVERSITÄT HAMBURG**

2023

Supervisor:

Professor Angel Rubio
Assitant Professor Shunsuke Sato

Examiners:

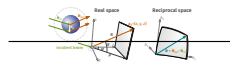
Professor YAN Jie
Associate Professor Andriyo RUSYDI
Assistant Professor WONG Liang Jie, Nanyang Technological University

EIDESSTATTLICHE VERSICHERUNG / DECLARATION

Hiermit versichere ich an Eides statt, die vorliegende Dissertationsschrift selbst verfasst und keine anderen als die angegebenen Hilfsmittel und Quellen benutzt zu haben.

Die eingereichte schriftliche Fassung entspricht der auf dem elektronischen Speichermedium.

Die Dissertation wurde in der vorgelegten oder einer ähnlichen Form nicht schon einmal in einem früheren Promotionsverfahren angenommen oder als ungenügend beurteilt.



Wenwen Mao
December 28, 2023

Acknowledgements

First, I would like to thank my supervisors Angel Rubio and Shunsuke Sato for their continuous support of my Ph.D

To my

Contents

| | |
|---|-------------|
| Acknowledgements | i |
| Contents | iii |
| Summary | v |
| List of Tables | vi |
| List of Figures | viii |
| List of Abbreviations | xi |
| 1 THEORETICAL FOUNDATIONS | 1 |
| 1.1 Crystallography properties | 1 |
| 1.1.1 Structural parameters | 2 |
| 1.1.2 Reciprocal space | 3 |
| 1.2 Tight-binding Approach | 3 |
| 1.3 Electron dynamics | 5 |
| 1.3.1 Time-dependent Schrödinger equation | 6 |
| 1.3.2 Quantum Master Equation | 8 |
| 2 CO-LINEAR POLARIZATION INDUCED PHOTOVOLTAIC EFFECT | 11 |
| 2.1 Time-dependent Perturbative Analysis on QuI | 12 |
| 2.2 Third-order Nonlinear Regime: $1 + 2$ QuIC | 20 |
| 2.3 Deeply off-resonant highly-nonlinear regime | 30 |
| A ADIABATIC BASIS REPRESENTATION | 39 |

Summary

Modeling Nonlinear Optical Response in 2D materials from Nonequilibrium
Quantum Dynamics

by

Wenwen Mao

der Fakultät für Mathematik, Informatik und Naturwissenschaften, Fachbereich
Physik
Universität Hamburg

Through the exploration of high-order harmonic generation, this research contributes to the broader scientific community's knowledge and paves the way for new discoveries and technological breakthroughs. The study of HHG not only deepens our comprehension of fundamental physics but also holds great promise for revolutionizing various fields, ranging from materials science and chemistry to biology and quantum technologies.

This page is intentionally left blank.

List of Tables

This page is intentionally left blank.

List of Figures

| | | |
|-----|--|----|
| 1.1 | Lab coordinate system | 2 |
| 2.1 | The time profiles of the electric field given by Eq. (2.39) are shown for (a) $\phi = 0$ and (b) $\phi = \pi/2$ | 22 |
| 2.2 | (a, b) The conduction population distribution $n_c(k)$ computed with (a) $\phi = 0$ and (b) $\phi = \pi/2$. (c, d) The population imbalance distribution $\Delta n_c(k)$ computed with (c) $\phi = 0$ and (d) $\phi = \pi/2$ | 23 |
| 2.3 | | 24 |
| 2.4 | The dc components of the currents $J_{dc}(t)$ computed from Eq. (2.40) are shown as a function of time. The results using the relative phase of $\phi = 0$ are shown in panel (a), while those using $\phi = \pi/2$ are shown in (b) | 25 |
| 2.5 | The persistent current $J_{dc}(t_f)$ as a function of the relative phase, ϕ . The results are computed by setting E_0 to 2.57 MV/cm and $\hbar\omega$ to 3 eV. | 27 |
| 2.6 | The current after the laser irradiation is shown as a function of the fundamental photon energy $\hbar\omega$. The results computed different field strengths: (a) $E_0 = 1.03$ MV/cm, (b) 51.43 MV/cm, and (c) $E_0 = 102.84$ MV/cm. | 28 |
| 2.7 | (a) The conduction population distribution $n_c(k)$ after the irradiation of the laser field, and (b) the population imbalance distribution $\Delta n_c(k)$ are shown. The results are computed by setting E_0 to 10^{10} V/m. | 35 |

| | | |
|------|--|----|
| 2.8 | The dc components of the currents, $J_{dc}(t)$, are shown as a function of time. The results are computed with the deeply off-resonant condition, $\hbar\omega = 1.0$ eV. | 36 |
| 2.9 | The persistent current, $J_{dc}(t_f)$, is shown as a function of the relative phase ϕ . The results are computed with the deeply off-resonant condition, $\hbar\omega = 1.0$ eV. | 36 |
| 2.10 | (a) The persistent current, $ J_{dc}(t_f) $, is shown as a function of the field strength, E_0 . (b) The number of conduction population after the laser irradiation is shown as a function of the field strength E_0 | 37 |

List of Abbreviations

| | |
|------|---|
| h-BN | Hexagonal boron nitride. 2 |
| QuI | Quantum Interference. 18 |
| QuIC | Quantum Interference Control. 20 , 21 , 26–32 |
| TDSE | Time-dependent Schrödinger equation. 6 , 20 |

This page is intentionally left blank.

THEORETICAL FOUNDATIONS

1.1 Crystallography properties

The hexagonal lattice nanostructure, a fundamental Bravais lattice, manifests as a distinctive geometric arrangement prevalent across a spectrum of materials, owing to its highly efficient packing characteristics. This lattice's spatial configuration profoundly influences the mechanical, electrical, and thermal properties of materials. Understanding lattice structures is crucial for deciphering material behavior across diverse conditions, spanning from semimetals to topological insulators. This significance is particularly noteworthy in the realm of two-dimensional materials. We have selected graphene, exemplifying a semimetal, and hexagonal boron nitride (h-BN), recognized as an insulator, for our discussion on nonlinear optical response on 2d materials.

Graphene, an extraordinary carbon allotrope, showcases a captivating atomic arrangement within a hexagonal lattice nanostructure, depicted in Figure 1.1 (a). Carbon atoms meticulously align in a single layer, forming an exceptional two-dimensional material. The unique atomic-scale hexagonal lattice structure involves each carbon atom intricately bonding through σ -bonds with its three nearest neighbors and a delocalized π -bond. This precise arrangement plays a pivotal role in the formation of a valence band elegantly spanning the entirety of the graphene sheet, making monolayer graphene an outstanding conductor of electricity, and finding applications in electronic devices, sensors, and various fields.

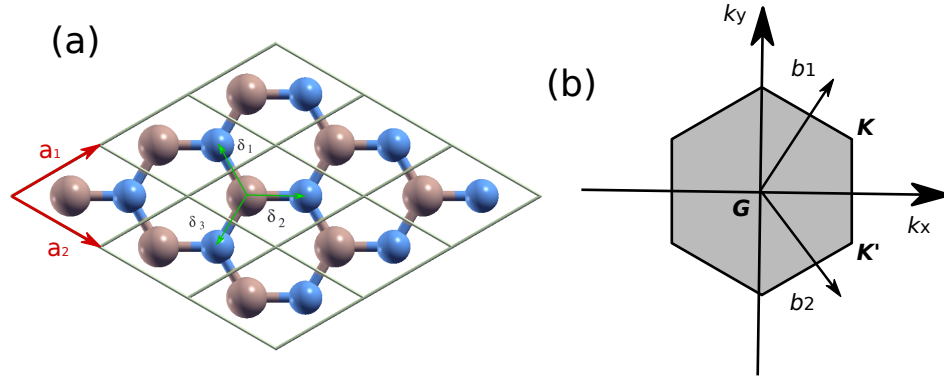


Figure 1.1: (a) Hexagonal lattice showing in different colors the two triangular sublattices. (b) Brillouin zone in momentum space.

Similar to graphene, Hexagonal boron nitride (**h-BN**) also features a hexagonal lattice structure, but with alternating boron and nitrogen atoms forming the hexagons, making it a wide-gap insulator due to inversion symmetry breaking, which is used as a dielectric material in electronics, a substrate for graphene-based devices, and as a solid lubricant.

1.1.1 Structural parameters

We define the basis of hexagonal lattice primitive vectors $E = (\vec{a}_1, \vec{a}_2)$ as shown in Fig 1.1 (a):

$$\vec{a}_1 = a \begin{pmatrix} \frac{\sqrt{3}}{2} \\ \frac{1}{2} \end{pmatrix}, \vec{a}_2 = a \begin{pmatrix} \frac{\sqrt{3}}{2} \\ -\frac{1}{2} \end{pmatrix}$$

Where a is the lattice constant, for graphene $a = 1.42 \text{ \AA}$ [1], and for **h-BN** $a = 2.5 \text{ \AA}$ [2]. Generate only A sites while sites in B sublattice are generated by $n_1 \vec{a}_1 + n_2 \vec{a}_2 + \vec{\delta}$, where $\vec{\delta}$ has to be chosen as one of the three nearest-neighbor vectors,

$$\vec{\delta}_1 = a \begin{pmatrix} -\frac{1}{2\sqrt{3}} \\ \frac{1}{2} \end{pmatrix}, \vec{\delta}_2 = a \begin{pmatrix} \frac{1}{\sqrt{3}} \\ 0 \end{pmatrix}, \vec{\delta}_3 = a \begin{pmatrix} -\frac{1}{2\sqrt{3}} \\ -\frac{1}{2} \end{pmatrix}$$

1.1.2 Reciprocal space

The reciprocal basis $B = (b_1, b_2, b_3)$ is generated using the formula:

$$\vec{b}_k = \frac{2\pi \cdot \vec{a}_i \times \vec{a}_j}{V}$$

i, j, k are circular permutations, V the mix product between the three vectors, i.e. the volume of the unitary cell. Then we get the 2D reciprocal vectors as shown in Fig 1.1 (b):

$$\vec{b}_1 = k_D \begin{pmatrix} \frac{1}{2} \\ \frac{\sqrt{3}}{2} \end{pmatrix}, \vec{b}_2 = k_D \begin{pmatrix} \frac{1}{2} \\ -\frac{\sqrt{3}}{2} \end{pmatrix}$$

And with $k_D = \frac{4\pi}{\sqrt{3}a}$. The corresponding Brillouin zone is depicted together with the two high-symmetry points K and K' Fig 1.1 (b). Two inequivalent corners of the Brillouin zone K and K' can be chosen as follows:

$$K = k_D \left(\frac{1}{2}, \frac{1}{2\sqrt{3}} \right), \quad K' = k_D \left(\frac{1}{2}, -\frac{1}{2\sqrt{3}} \right)$$

1.2 Tight-binding Approach

In this section, we delve into the fundamental principles of the tight-binding approach, with a particular focus on the nearest neighbor tight-binding model. This approach is essential for understanding the electronic properties of materials and is a crucial component of graphene's electronic structure analysis.

The foundation of the tight-binding approach is rooted in the Bloch theorem, which is satisfied by the tight-binding function

$$\Phi_\alpha(\mathbf{r}, \mathbf{k}) = \frac{1}{\sqrt{N}} \sum_{\mathbf{R}} e^{i\mathbf{k} \cdot \mathbf{R}} \phi_\alpha(\mathbf{r} - \mathbf{R}_\alpha), \alpha = A \text{ or } B \quad (1.1)$$

Here, N represents the number of unit cells, and $\phi_\alpha(\mathbf{r} - \mathbf{R}_\alpha)$ denotes the orbital function of an electron at cell \mathbf{R} in sublattice α . In the context of a honeycomb lattice, we focus on the nearest neighbor approximation. This approximation asserts that an atom in sublattice A only interacts with its three closest neighbor atoms in sublattice B. This simplification is particularly useful for understanding the interactions between electrons bound to non-equivalent atoms.

The Hamiltonian operator for this nearest-neighbor interaction is expressed as:

$$\hat{H}_{AB} = \frac{1}{N} \sum_{\mathbf{R}_A} \sum_{\mathbf{R}_B} e^{i\mathbf{k}(\mathbf{R}_B - \mathbf{R}_A)} \langle \phi_A(\mathbf{r} - \mathbf{R}_A) | \hat{H} | \phi_B(\mathbf{r} - \mathbf{R}_B) \rangle \quad (1.2)$$

Due to the translational invariance in a Bravais lattice, the summation over each atom in a sublattice occurs N times, simplifying the expression to:

$$\hat{H}_{AB} = \sum_{\mathbf{R}_A} e^{i\mathbf{k}(\mathbf{R}_B - \mathbf{R}_A)} \langle \phi_A(\mathbf{r} - \mathbf{R}_A) | \hat{H} | \phi_B(\mathbf{r} - \mathbf{R}_B) \rangle \quad (1.3)$$

To transition from real space to momentum space, we employ a Fourier transform, allowing us to represent the Hamiltonian in terms of momentum space. This transformation results in the tight-binding Hamiltonian under the momentum representation, as defined by:

$$c_{\mathbf{R}_\alpha, \sigma} = \frac{1}{\sqrt{N}} \sum_{\mathbf{k}} e^{i\mathbf{k} \cdot \mathbf{R}_\alpha} c_{\mathbf{k}, \sigma} \quad (1.4)$$

$$c_{\mathbf{R}_\alpha, \sigma}^\dagger = \frac{1}{\sqrt{N}} \sum_{\mathbf{k}} e^{-i\mathbf{k} \cdot \mathbf{R}_\alpha} c_{\mathbf{k}, \sigma}^\dagger \quad (1.5)$$

$\sigma = \uparrow, \downarrow$ presents the electron spin, With the orthogonal normalization conditions

$$\delta_{\mathbf{k}\mathbf{k}'} = \frac{1}{N} \sum_{\mathbf{R}_\alpha} e^{i(\mathbf{k} - \mathbf{k}') \cdot \mathbf{R}_\alpha} \quad (1.6)$$

We transform the Hamiltonian of real space into the momentum space representation, and then the tight-binding Hamiltonian under the momentum representation is:

$$\hat{H} = \begin{pmatrix} \epsilon_A & t_0 f(\mathbf{k}) \\ t_0 f(\mathbf{k})^* & \epsilon_B \end{pmatrix} \quad (1.7)$$

Here ϵ_A and ϵ_B are the on-site energies of electrons on the nearest neighbor atoms, t_0 presents the hopping parameter:

$$t_0 = \langle \phi_A(\mathbf{r} - \mathbf{R}_A) | \hat{H} | \phi_B(\mathbf{r} - \mathbf{R}_A - \vec{\delta}_i) \rangle \quad (i = 1, 2, 3)$$

For graphene, we set ϵ_A and ϵ_B to 0, and $t_0 = 2.8 \text{ eV}$ in accordance with the pre-

vious work [1]. For h-BN ϵ_B and ϵ_N denote the on-site energies for boron and nitrogen sites, respectively.

$$\hat{H}(\mathbf{k}) = \begin{pmatrix} \epsilon_B & t_0 f(\mathbf{k}) \\ t_0 f(\mathbf{k})^* & \epsilon_N \end{pmatrix}, \quad (1.8)$$

We set ϵ_B to 3.34 eV and ϵ_N to -2.56 eV and t_0 to 2.6 eV computed with the first-principles calculations [3], the band gap $E_g = \epsilon_b - \epsilon_n$ equals 5.9 eV.

The off-diagonal terms of the tight-binding Hamiltonian 1.7:

$$\begin{aligned} f(\mathbf{k}) &= e^{i\mathbf{k}\vec{\delta}_1} + e^{i\mathbf{k}\vec{\delta}_2} + e^{i\mathbf{k}\vec{\delta}_3} \\ &= e^{-\frac{iak_x}{\sqrt{3}}} + 2e^{\frac{iak_x}{2\sqrt{3}}} \cos\left(\frac{a}{2}k_y\right) \end{aligned} \quad (1.9)$$

Solving the stationary Schrödinger equation using matrix diagonalization:

$$\hat{H}_k |\phi_{bk}\rangle = \epsilon_{bk} |\phi_b\rangle, \quad (1.10)$$

We get the eigenenergy of Hamiltonian from 1.7, where b is a band index, $|\phi_{bk}\rangle$ is an eigenstate, and ϵ_{bk} corresponds to the eigenenergy. As the Hamiltonian is a 2-by-2 matrix in this work, the band index b denotes either a conduction ($b = c$) or valence ($b = v$) state.

$$\epsilon_{bk} = E_0 \pm \frac{1}{2} \sqrt{E_g^2 + 4t_0^2 |f|^2} \quad (1.11)$$

$E_0 = \frac{\epsilon_A + \epsilon_B}{2}$ and $E_g = \epsilon_b - \epsilon_n$ is the energy gap. For graphene, $\epsilon_A = \epsilon_B = 0$ the band gap equals 0. Their corresponding eigenvectors are:

$$|\phi_b\rangle = \begin{pmatrix} \frac{E_g \pm \sqrt{E_g^2 + 4t_0^2 |f|^2}}{2t_0 f^*} \\ 1 \end{pmatrix} \quad (1.12)$$

1.3 Electron dynamics

Consider the crystal under the electric field E , to avoid that Bloch's theorem cannot be applied, let the electric field enter through a uniform vector potential $A(t)$.

The time-dependent Hamiltonian is written as

$$\hat{H}(t) = \frac{[\hat{p} + eA(t)]^2}{2m} + V(r) \quad (1.13)$$

Transforming to the k -space representation, we have

$$\hat{H}(k, t) = \hat{H} \left(k + \frac{e}{\hbar} A(t) \right) \quad (1.14)$$

where k denotes the Bloch wavevector, and $|\psi_k(t)\rangle$ is a single-particle electronic wavefunction at k . The vector potential $A(t)$ is related to the applied electric field $E(t)$ as $E(t) = -dA(t)/dt$, and it is included in the Hamiltonian as the wavevector shift $k \rightarrow k + eA(t)/\hbar$ via the Peierls substitution [4].

1.3.1 Time-dependent Schrödinger equation

The light-induced electron dynamics can be described by solving the following time-dependent Schrödinger equation (TDSE) at each k -point:

$$i\hbar \frac{d}{dt} |\psi_k(t)\rangle = \hat{H} \left(k + \frac{eA(t)}{\hbar} \right) |\psi_k(t)\rangle, \quad (1.15)$$

Solving this time-dependent Schrödinger equation (TDSE) is an initial value problem. In two-band systems, usually the ground state $\psi_k(0)$ is used as the initial state occupied at the valence band with:

$$\psi_k(0) = \begin{pmatrix} 0 \\ 1 \end{pmatrix} \quad (1.16)$$

The adiabatic approximation is used almost all the time in solving time-propagation, which will be explained in more detail in the appendix A. Various numerical schemes can be chosen for doing the time propagation, here we split the propagation into short-time propagation using the composition property:

$$|\psi_k(t')\rangle = \exp \left[-i \int_t^{t'} d\tau \hat{H}(\tau) \right] |\psi_{k+A(t)}\rangle \quad (1.17)$$

In practice, simpler schemes are usually used and self-consistency is often neglected. Instead, we rely on a sufficiently small Δt , $t' = t + \Delta t$, the exponential mid-point propagator is given by:

$$U(t + \Delta t, t) \approx U_{EM}(t + \Delta t, t) = \exp\{-i\Delta t \hat{H}(t + \Delta t/2)\} \quad (1.18)$$

We approximate the exponential using a Taylor expansion to fourth-order:

$$\exp\{A\} = \sum_{k=0}^{\infty} \frac{1}{k!} A^k \quad (1.19)$$

Once the time-evolution of the wavefunctions, $|\psi_k(t)\rangle$ is computed, the current induced in the matter can be further evaluated with

$$J_k(t) = \frac{1}{(2\pi)^2} \int_{BZ} dk \langle \psi_k(t) | \hat{J}_k(t) | \psi_k(t) \rangle. \quad (1.20)$$

Here, $\hat{J}_k(t)$ is the current operator, and it is defined as

$$\hat{J}_k(t) = \frac{\partial}{\partial k} \hat{H} \left(k + \frac{eA(t)}{\hbar} \right) = -t_0 \begin{pmatrix} 0 & \frac{\partial f(k+A)}{\partial A} \\ \frac{\partial f^*(k+A)}{\partial A} & 0 \end{pmatrix}, \quad (1.21)$$

where $\frac{\partial f(k)}{\partial k}$ is given by

$$\frac{\partial f(k)}{\partial k} = i\delta_1 e^{ik \cdot \delta_1} + i\delta_2 e^{ik \cdot \delta_2} + i\delta_3 e^{ik \cdot \delta_3}. \quad (1.22)$$

Current 1.20 can be further decomposed into:

$$\begin{aligned} J_{b,k}(t) &= \langle \psi_{b,k}(t) | J(t) | \psi_{b,k}(t) \rangle \\ &= \sum_{b',b''} c_{b',k}(t) c_{b'',k}^*(t) \langle \phi_{b'',k}^H(t) | J(t) | \phi_{b',k}^H(t) \rangle + \sum_{b',b''} |c_{b',k}(t)|^2 \langle \phi_{b',k}^H(t) | J(t) | \phi_{b',k}^H(t) \rangle \end{aligned} \quad (1.23)$$

Here the off-diagonal terms contribute to the Interband current, and the diagonal terms contribute to the Intraband current.

$$J_{inter;b,k}(t) = \sum_{b',b''} c_{b',k}(t) c_{b'',k}^*(t) \langle \phi_{b'',k}^H(t) | J(t) | \phi_{b',k}^H(t) \rangle \quad (1.24)$$

$$J_{intra;b,k}(t) = \sum_{b',b''} |c_{b'k}(t)|^2 \langle \phi_{b'k}^H(t) | J(t) | \phi_{b'k}^H(t) \rangle \quad (1.25)$$

By combining time-dependent wavefunction $\psi_k(t)$ solved from Eq. (1.7) and the eigenstates ϕ_{ck} defined with Eq. (1.10), the conduction population distribution n_{ck} with the laser irradiation at instantaneous time t can be evaluated as:

$$n_{ck} = |\langle \phi_{ck} | \psi_k(t) \rangle|^2, \quad (1.26)$$

$\frac{\partial \epsilon_{b,k+A(t)}}{\partial k} = -\langle \phi_{b'k}^H(t) | J(t) | \phi_{b'k}^H(t) \rangle$ defines the band velocity. The eigenenergy of conduction band at time t is $\epsilon_{c,k+A(t)} = E_0 + \frac{1}{2} \sqrt{E_g^2 + 4t_0^2 |f(k+A(t))|^2}$

$$\frac{\partial \epsilon_{v,k+A(t)}}{\partial k} = -\frac{t_0^2}{2\epsilon_{v,k+A(t)} - (\epsilon_b + \epsilon_n)} \cdot (f^*(k+A(t)) \frac{\partial f(k+A(t))}{\partial k} + c.c.) \quad (1.27)$$

$$\frac{\partial \epsilon_{c,k+A(t)}}{\partial k} = \frac{t_0^2}{2\epsilon_{c,k+A(t)} - (\epsilon_b + \epsilon_n)} \cdot (f^*(k+A(t)) \frac{\partial f(k+A(t))}{\partial k} + c.c.) \quad (1.28)$$

1.3.2 Quantum Master Equation

In contrast to closed quantum systems, which are entirely isolated from external influences and can be adequately described by the Schrödinger equation, the quantum master equation is typically used in the context of the time evolution of an open quantum system, where the system of interest is susceptible to exchanges of energy, particles, or information with its external environment. To expound processes such as relaxation, dephasing, and thermalization of the nonlinear response experiments, the quantum master equation is predominantly employed which is salient in the realm of open quantum systems.

We describe the light-induced electron dynamics in graphene with the following quantum master equation [5–8]:

$$\frac{d}{dt} \rho_k(t) = \frac{1}{i\hbar} [\hat{H}_{k+eA(t)/\hbar}, \rho_k(t)] + \hat{D}[\rho_k(t)], \quad (1.29)$$

$\rho_k(t)$ is the reduced density matrix at k . The quantum master equation delineates the dynamical evolution of the density matrix associated with the quantum system, which encompasses both pure and mixed quantum states. To elucidate the impact of dissipation, we formulate the relaxation operator, denoted as $\hat{D}[\rho_k(t)]$, within the framework of Eq.(1.29) employing the relaxation time approximation[9] and employing the Houston basis [10, 11]. The Houston states are characterized as eigenstates of the instantaneous Hamiltonian, expressed as:

$$\hat{H}_{k+eA(t)/\hbar}|u_{bk}^H(t)\rangle = \epsilon_{b,k+eA(t)/\hbar}|u_{bk}^H(t)\rangle \quad (1.30)$$

The expansion of the reduced density matrix can then be carried out using the Houston states.

$$\rho_k(t) = \sum_{bb'} \rho_{bb',k}(t) |u_{bk}^H(t)\rangle \langle u_{b'k}^H(t)|, \quad (1.31)$$

where $\rho_{bb',k}(t)$ are the expansion coefficients. On the basis of the Houston state expansion, we define the relaxation operator [5, 6, 12] as

$$\hat{D}[\rho_k(t)] = - \sum_b \frac{\rho_{bb,k}(t) - f^{FD}(\epsilon_{b,k+eA(t)/\hbar}, T_e, \mu)}{T_1} |u_{bk}^H(t)\rangle \langle u_{bk}^H(t)| - \sum_{b \neq b'} \frac{\rho_{bb',k}(t)}{T_2} |u_{bk}^H(t)\rangle \langle u_{b'k}^H(t)|, \quad (1.32)$$

T_1 is the longitudinal relaxation time, T_2 is the transverse relaxation time, and $f^{FD}(\epsilon)$ is the Fermi–Dirac distribution

$$f^{FD}(\epsilon, T_e, \mu) = \frac{1}{e^{(\epsilon-\mu)/k_B T_e} + 1}. \quad (1.33)$$

μ is the chemical potential, and T_e is the electron temperature. In the following discussion, we set the longitudinal relaxation time T_1 to 100 fs and the transverse relaxation time T_2 to 20 fs in accordance with the previous works [5–8]. The electron temperature T_e is set to 300 K unless stated otherwise. The chemical potential μ is treated as a tunable parameter to study the effect of doping.

We directly solve the quantum master equation, Eq. (1.29), in the time domain by employing the Runge-Kutta method without any approximation. The electric current is obtained by employing the time-dependent density matrix $\rho_k(t)$, which

evolves according to Eq. (1.29):

$$J(t) = \frac{2}{(2\pi)^2} \int dk \text{Tr} [\hat{J}_k(t) \rho_k(t)], \quad (1.34)$$

where $\hat{J}_k(t)$ is the current operator defined as

$$\hat{J}_k(t) = -\frac{\partial H(k + eA(t)/\hbar)}{\partial A(t)}. \quad (1.35)$$

The intraband component of the current is

$$J_k^{\text{intra}}(t) = \sum_{b=v,c} \frac{(-2)}{(2\pi)^2} \frac{e}{\hbar} \times \int dk \frac{\partial \epsilon_{b,k+eA(t)/\hbar}}{\partial k} n_{b,k+eA(t)/\hbar},$$

where the band population $n_{b,k+eA(t)/\hbar}$ is defined with the Houston states of the Hamiltonian $|u_{b,k}^H(t)\rangle$ computed from Eq 1.30:

$$n_{b,k+eA(t)/\hbar}(t) = \langle u_{b,k}^H(t) | \rho_k(t) | u_{b,k}^H(t) \rangle \quad (1.36)$$

CO-LINEAR POLARIZATION INDUCED PHOTOVOLTAIC EFFECT

Addressing the photovoltaic effect within the perturbative regime has garnered significant attention, particularly in the exploration of dc current injection using two-color linearly polarized light [13–19]. Early investigations have underscored the intricate interplay between a fundamental frequency, denoted as ω , and its second harmonic, 2ω [13–15]. A notable study by Jimenez-Galan et al. [20] utilized deeply off-resonant bi-circular laser fields with frequencies ω and 2ω to generate a substantial population imbalance in the Brillouin zone. However, it is worth noting that, in principle, the use of linearly polarized light with two frequencies is sufficient to break time-reversal symmetry.

In this Chapter, we first theoretically explore the phenomenon of dc-current injection and the generation of population imbalance through the application of two-color linearly polarized laser fields with frequencies ω and 2ω based on time-dependent perturbation analysis. To ground our analysis, we scrutinize light-induced electron dynamics in a prototypical two-dimensional material, monolayer hexagonal boron-nitride (*h*-BN), leveraging a simple tight-binding approximation first in a perturbative resonant regime.

In our quantum dynamics simulations, we further uncover that ballistic current can be induced even in the deeply off-resonant regime with two-color linearly polarized light. Consequently, efficient injection of dc-current and the cre-

ation of a substantial population imbalance can be realized by employing two-color linearly polarized laser fields with frequencies ω and 2ω , without relying on the ellipticity of light. These findings offer a potential pathway for achieving ultrafast and efficient control of electron population in matter using multi-color linearly polarized light, opening new avenues for exploring the frontiers of quantum dynamics and optoelectronic applications. This streamlined approach offers a promising avenue for achieving efficient and controlled current injection under conditions of deep off-resonance, potentially opening up new possibilities for nonlinear optoelectronic applications.

2.1 Time-dependent Perturbative Analysis on Qul

Time-dependent perturbation theory provides a formalism for describing the response of quantum systems to time-varying external fields, making it well-suited for analyzing the interaction of materials with intense electromagnetic radiation. It provides a formalism for describing the response of quantum systems to time-varying external fields, making it well-suited for analyzing the interaction of materials with intense electromagnetic radiation. Exploring the photovoltaic effect within the perturbative regime has led to a notable focus on elucidating the injection of direct current (dc) through the use of two-color linearly polarized light [13–19]. Here, we investigate the nonlinear photocarrier injection process via the time-dependent perturbation analysis. Under adiabatic basis representation described in Appendix A, one can rewrite the equation of motion for the coefficient vector as

$$\begin{aligned}
 i \frac{d}{dt} c_k(t) = & \\
 iE(t) \cdot & \begin{pmatrix} 0 & e^{-i \int_0^t dt' \Delta \epsilon_{cv,k+A(t')} + i \Delta \phi_{cv,k}^g(t)} \left\langle u_{v,k+A(t)} \left| \frac{\partial u_{c,k+A(t)}}{\partial k} \right\rangle \right. \\ e^{-i \int_0^t dt' \Delta \epsilon_{vc,k+A(t')} + i \Delta \phi_{vc,k}^g(t)} \left\langle u_{c,k+A(t)} \left| \frac{\partial u_{v,k+A(t)}}{\partial k} \right\rangle & 0 \end{pmatrix} c_k(t) \\
 = \mathcal{H}(t) c_k(t). & \quad (2.1)
 \end{aligned}$$

$c_k(t) = \begin{pmatrix} c_{v,k}(t) \\ c_{c,k}(t) \end{pmatrix}$ is the coefficient vector, $\Delta \epsilon_{bb',k+A(t)}$ is defined by the difference of the single-particle energies as $\epsilon_{b,k+A(t)} - \epsilon_{b',k+A(t)}$. For simplicity, here

2.1. TIME-DEPENDENT PERTURBATIVE ANALYSIS ON QUI

assume that the contributions from the geometric phases, $\Delta\phi_{cv,k}^g(t)$ are zero. Then expand the Hamiltonian in Eq. (A.10) up to the second order of the field $A(t)$ as

$$\mathcal{H}(t) \approx \mathcal{H}^{(1)}(t) + \mathcal{H}_{dyn}^{(2)}(t) + \mathcal{H}_{dip}^{(2)}(t), \quad (2.2)$$

$$\mathcal{H}^{(1)}(t) = iE(t) \cdot \begin{pmatrix} 0 & e^{-i\Delta\epsilon_{cv,k}t} \left\langle u_{v,k} \left| \frac{\partial u_{c,k}}{\partial k} \right\rangle \right. \\ e^{-i\Delta\epsilon_{vc,k}t} \left\langle u_{c,k} \left| \frac{\partial u_{v,k}}{\partial k} \right\rangle & 0 \end{pmatrix}, \quad (2.3)$$

$\mathcal{H}_{dyn}^{(2)}(t)$ and $\mathcal{H}_{dip}^{(2)}(t)$, are given by

$$\mathcal{H}_{dyn}^{(2)}(t) = E(t) \cdot \begin{pmatrix} 0 & \frac{\partial \Delta\epsilon_{cv,k}}{\partial k} \cdot \left(\int_0^t dt' A(t') \right) e^{-i\Delta\epsilon_{cv,k}t} \left\langle u_{v,k} \left| \frac{\partial u_{c,k}}{\partial k} \right\rangle \\ \frac{\partial \Delta\epsilon_{vc,k}}{\partial k} \cdot \left(\int_0^t dt' A(t') \right) e^{-i\Delta\epsilon_{vc,k}t} \left\langle u_{c,k} \left| \frac{\partial u_{v,k}}{\partial k} \right\rangle & 0 \end{pmatrix} \quad (2.4)$$

and

$$\mathcal{H}_{dip}^{(2)}(t) = \begin{pmatrix} 0 & e^{-i\Delta\epsilon_{cv,k}t} A(t) \cdot \frac{\partial u_{v,k} \left| iE(t) \cdot \frac{\partial u_{c,k}}{\partial k} \right.}{\partial k} \\ e^{-i\Delta\epsilon_{vc,k}t} A(t) \cdot \frac{\partial u_{c,k} \left| iE(t) \cdot \frac{\partial u_{v,k}}{\partial k} \right.}{\partial k} & 0 \end{pmatrix}. \quad (2.5)$$

Here, $\mathcal{H}_{dyn}^{(2)}(t)$ originates from the modification of the dynamical phase factor:

$$e^{-i \int_0^t dt' \Delta\epsilon_{vc,k+A(t')} } \quad (2.6)$$

while $\mathcal{H}_{dip}^{(2)}(t)$ originates from the modification of the dipole matrix elements:

$$i \left\langle u_{v,k+A(t)} \left| \frac{\partial u_{c,k+A(t)}}{\partial k} \right\rangle \quad (2.7)$$

Hereafter, we analyze the photocarrier injection process based on this perturba-

tive expansion of the Hamiltonian. Use perturbation expansion of Eq. (A.10):

$$i \frac{d}{dt} (c_k^{(0)}(t) + c_k^{(1)}(t) + c_k^{(2)}(t)) = (\mathcal{H}_k^{(0)} + \mathcal{H}_k^{(1)}(t) + \mathcal{H}_k^{(2)}(t)) (c_k^{(0)}(t) + c_k^{(1)}(t) + c_k^{(2)}(t)) \quad (2.8)$$

Under initial condition $\mathcal{H}_k^{(0)}(t=0) = 0$, $c_k^{(0)}(t=0) = \begin{pmatrix} 1 \\ 0 \end{pmatrix}$, the first and second-order coefficient vectors for the conduction band can be written as:

$$c_{c,k}^{(1)}(t) = \left\langle u_{c,k} \left| \frac{\partial u_{v,k}}{\partial k} \right. \right\rangle \int_0^t dt' e^{-i\Delta\epsilon_{vc,k}t'} E_1(t') \quad (2.9)$$

$$c_{c,k,dyn}^{(2)}(t) = \frac{1}{i} \frac{\partial \Delta\epsilon_{vc,k}}{\partial k} \left\langle u_{c,k} \left| \frac{\partial u_{v,k}}{\partial k} \right. \right\rangle \int_0^t dt' e^{-i\Delta\epsilon_{vc,k}t'} E_2(t') \int_0^{t'} dt'' A_2(t'') \quad (2.10)$$

$$c_{c,k,dip}^{(2)}(t) = \frac{\partial \left\langle u_{c,k} \left| \frac{\partial u_{v,k}}{\partial k} \right. \right\rangle}{\partial k} \int_0^t dt' e^{-i\Delta\epsilon_{vc,k}t'} E_2(t') A_2(t') \quad (2.11)$$

Under two-color linearly polarized light, here we consider the perturbation by the external linearly polarized vector potential for \vec{e} -direction, assuming that the perturbation only exists time between 0 and T_0 under the Gaussian distribution:

$$f(t) = e^{-\frac{(t-T_0)^2}{2\sigma^2}} \quad (2.12)$$

$$A_1(t) = A_1 \vec{e} \cos[2w(t - T_0) + \phi] e^{-\frac{(t-T_0)^2}{2\sigma^2}}, \quad (2.13)$$

$$A_2(t) = A_2 \vec{e} \cos[w(t - T_0)] e^{-\frac{(t-T_0)^2}{2\sigma^2}} \quad (2.14)$$

w is the carrier frequency of the field, \vec{e} represents a unit vector along the polarization direction of the laser field. We assume $T_0 \gg 0$ and $\sigma \gg 0$ to make the approximation:

$$\int_0^t A_2 \vec{e} \cos[w(t - T_0)] e^{-\frac{(t-T_0)^2}{2\sigma^2}} = \frac{A_2 \vec{e}}{w} \sin[w(t' - T_0)] e^{-\frac{(t'-T_0)^2}{2\sigma^2}} \quad (2.15)$$

2.1. TIME-DEPENDENT PERTURBATIVE ANALYSIS ON QUI

The corresponding external electric field $E(t) = -dA(t)/dt$ can be written as the following pulsed form:

$$E_1(t) = 2wA_1\vec{e}\sin[2w(t - T_0) + \phi]e^{-\frac{(t-T_0)^2}{2\sigma^2}}, \quad (2.16)$$

$$E_2(t) = wA_2\vec{e}\sin[w(t - T_0)]e^{-\frac{(t-T_0)^2}{2\sigma^2}} \quad (2.17)$$

Now, let's express this in terms of the first-order coefficient vector is:

$$\begin{aligned} c_{c,k}^{(1)}(t) &= \left\langle u_{c,k} \left| \frac{\partial u_{v,k}}{\partial k} \right. \right\rangle \int_0^t dt' e^{-i\Delta\epsilon_{vc,k}t'} 2wA_1\vec{e} \cdot \sin[2w(t' - T_0) + \phi] e^{-\frac{(t'-T_0)^2}{2\sigma^2}} \\ &= \frac{A_1\vec{e}w}{i} \left\langle u_{c,k} \left| \frac{\partial u_{v,k}}{\partial k} \right. \right\rangle \int_0^t dt' e^{-i\Delta\epsilon_{vc,k}t' - \frac{(t'-T_0)^2}{2\sigma^2}} \cdot (e^{i[2w(t'-T_0)+\phi]} - e^{-i[2w(t'-T_0)+\phi]}) \end{aligned} \quad (2.18)$$

We consider the population distribution after the laser pulse, so we replace the integra \int_0^t by $\int_{-\infty}^{\infty}$. Under the Gaussian integral,

$$\int_{-\infty}^{\infty} e^{-x^2} dx = \sqrt{\pi} \quad (2.19)$$

we get:

$$c_{c,k}^{(1)}(t) = \frac{A_1\vec{e}w \cdot \sigma\sqrt{2\pi}}{i} \left\langle u_{c,k} \left| \frac{\partial u_{v,k}}{\partial k} \right. \right\rangle \cdot e^{-i\Delta\epsilon_{vc,k}T_0} [e^{-\frac{1}{2}(\Delta\epsilon_{vc,k}-2w)^2\sigma^2-i\phi} - e^{-\frac{1}{2}(\Delta\epsilon_{vc,k}+2w)^2\sigma^2+i\phi}] \quad (2.20)$$

Similarly to the first-order perturbation coefficient vector's derivation, the second-order coefficient $c_{c,k}^{(2)}(t)$ can be written as:

$$c_{c,k,dyn}^{(2)}(t) = \frac{(A_2\vec{e})^2 \cdot \sigma\sqrt{\pi}}{2i} \frac{\partial \Delta\epsilon_{vc,k}}{\partial k} \left\langle u_{c,k} \left| \frac{\partial u_{v,k}}{\partial k} \right. \right\rangle \cdot e^{-i\Delta\epsilon_{vc,k}T_0} \cdot [e^{-\frac{\sigma^2}{4}\Delta\epsilon_{vc,k}^2} - \frac{1}{2}(e^{-\frac{\sigma^2}{4}(\Delta\epsilon_{vc,k}-2w)^2} + e^{-\frac{\sigma^2}{4}(\Delta\epsilon_{vc,k}+2w)^2})] \quad (2.21)$$

$$c_{c,k,dip}^{(2)}(t) = \frac{(A_2\vec{e})^2 w \cdot \sigma\sqrt{\pi}}{4i} \cdot \frac{\partial \left\langle u_{c,k} \left| \frac{\partial u_{v,k}}{\partial k} \right. \right\rangle}{\partial k} \cdot e^{-i\Delta\epsilon_{vc,k}T_0} [e^{-\frac{\sigma^2}{4}(\Delta\epsilon_{vc,k}-2w)^2} - e^{-\frac{\sigma^2}{4}(\Delta\epsilon_{vc,k}+2w)^2}] \quad (2.22)$$

This completes the derivation of the population of the conduction band after the

laser pulse:

$$\begin{aligned}
 |c_{c,k}(t)|^2 &= |c_{c,k}^{(1)}(t)|^2 + |c_{c,k,dyn}^{(2)}(t)|^2 + |c_{c,k,dip}^{(2)}(t)|^2 \\
 &\quad + c_{c,k}^{(1)}(t)^* c_{c,k,dyn}^{(2)}(t) + c.c. \\
 &\quad + c_{c,k}^{(1)}(t)^* c_{c,k,dip}^{(2)}(t) + c.c. \\
 &\quad + c_{c,k,dyn}^{(2)}(t)^* c_{c,k,dip}^{(2)}(t) + c.c.
 \end{aligned} \tag{2.23}$$

We consider a prototypical two-dimensional insulator, monolayer hexagonal boron-nitride (*h*-BN). For the 2-band hBN-tight-binding model, the inversion symmetric is breaking:

$$u_k(-\vec{r}) \neq u_{-k}(\vec{r}) \tag{2.24}$$

We apply the time-reversal relation for the derivation:

$$u_k^*(\vec{r}) = u_{-k}(\vec{r}) \tag{2.25}$$

To compare the $|c_{c,-k}(t)|^2$, the absolute value of the coefficient becomes:

$$\begin{aligned}
 |c_{c,k}^{(1)}(t)|^2 &= \left| \frac{A_1 \vec{e} w \cdot \sigma \sqrt{2\pi}}{i} \left\langle u_{c,k} \left| \frac{\partial u_{v,k}}{\partial k} \right. \right\rangle \right|^2 \\
 &\quad \cdot [e^{-(\Delta\epsilon_{vc,k}-2w)^2\sigma^2} + e^{-(\Delta\epsilon_{vc,k}+2w)^2\sigma^2} - 2e^{-\frac{1}{2}((\Delta\epsilon_{vc,k}-2w)^2\sigma^2 + (\Delta\epsilon_{vc,k}+2w)^2\sigma^2)} \cos(2\phi)] \\
 &= |c_{c,-k}^{(1)}(t)|^2
 \end{aligned} \tag{2.26}$$

$$\begin{aligned}
 |c_{c,k,dyn}^{(2)}(t)|^2 &= \left| \frac{(A_2 \vec{e})^2 w \cdot \sigma \sqrt{\pi}}{2} \frac{\partial \Delta\epsilon_{vc,k}}{\partial k} \left\langle u_{c,k} \left| \frac{\partial u_{v,k}}{\partial k} \right. \right\rangle \cdot [e^{-\frac{\sigma^2}{4} \Delta\epsilon_{vc,k}^2} - \frac{1}{2}(e^{-\frac{\sigma^2}{4}(\Delta\epsilon_{vc,k}-2w)^2} + e^{-\frac{\sigma^2}{4}(\Delta\epsilon_{vc,k}+2w)^2})] \right|^2 \\
 &= |c_{c,-k,dyn}^{(2)}(t)|^2
 \end{aligned} \tag{2.27}$$

$$\begin{aligned}
 |c_{c,k,dip}^{(2)}(t)|^2 &= \left| \frac{(A_2 \vec{e})^2 w \cdot \sigma \sqrt{\pi}}{4} \cdot \frac{\partial \left\langle u_{c,k} \left| \frac{\partial u_{v,k}}{\partial k} \right. \right\rangle}{\partial k} [e^{-\frac{\sigma^2}{4}(\Delta\epsilon_{vc,k}-2w)^2} - e^{-\frac{\sigma^2}{4}(\Delta\epsilon_{vc,k}+2w)^2}] \right|^2 \\
 &= |c_{c,-k,dip}^{(2)}(t)|^2
 \end{aligned} \tag{2.28}$$

2.1. TIME-DEPENDENT PERTURBATIVE ANALYSIS ON QUI

The interference terms are:

$$\begin{aligned}
c_{c,k}^{(1)}(t)^* c_{c,k,dyn}^{(2)}(t) + c.c. &= \sqrt{2} A_1 A_2^2 \vec{e} w \cdot \sigma^2 \pi \frac{\partial \Delta \epsilon_{vc,k}}{\partial k} \left| \left\langle u_{c,k} \left| \frac{\partial u_{v,k}}{\partial k} \right\rangle \right|^2 \\
&\cdot \left[e^{-\frac{\sigma^2}{4} \Delta \epsilon_{vc,k}^2} - \frac{1}{2} (e^{-\frac{\sigma^2}{4} (\Delta \epsilon_{vc,k} - 2w)^2} + e^{-\frac{\sigma^2}{4} (\Delta \epsilon_{vc,k} + 2w)^2}) \right] \\
&\cdot [e^{-\frac{1}{2} (\Delta \epsilon_{vc,k} - 2w)^2 \sigma^2} - e^{-\frac{1}{2} (\Delta \epsilon_{vc,k} + 2w)^2 \sigma^2}] \cos \phi \\
&= -(c_{c,-k}^{(1)}(t)^* c_{c,-k,dyn}^{(2)}(t) + c.c.)
\end{aligned} \tag{2.29}$$

$$\begin{aligned}
c_{c,k}^{(1)}(t)^* c_{c,k,dip}^{(2)}(t) + c.c. &= \frac{\sqrt{2} A_1 A_2^2 \vec{e} w^2 \cdot \sigma^2 \pi}{4} \cdot (e^{-\frac{\sigma^2}{4} (\Delta \epsilon_{vc,k} - 2w)^2} - e^{-\frac{\sigma^2}{4} (\Delta \epsilon_{vc,k} + 2w)^2}) \\
&\cdot \left(\left\langle \frac{\partial u_{v,k}}{\partial k} \left| u_{c,k} \right\rangle \frac{\partial \left\langle u_{c,k} \left| \frac{\partial u_{v,k}}{\partial k} \right\rangle}{\partial k} [e^{-\frac{1}{2} (\Delta \epsilon_{vc,k} - 2w)^2 \sigma^2 + i\phi} - e^{-\frac{1}{2} (\Delta \epsilon_{vc,k} + 2w)^2 \sigma^2 - i\phi}] \right. \right. \\
&\left. \left. + \frac{\partial \left\langle \frac{\partial u_{v,k}}{\partial k} \left| u_{c,k} \right\rangle}{\partial k} \left\langle u_{c,k} \left| \frac{\partial u_{v,k}}{\partial k} \right\rangle [e^{-\frac{1}{2} (\Delta \epsilon_{vc,k} - 2w)^2 \sigma^2 - i\phi} - e^{-\frac{1}{2} (\Delta \epsilon_{vc,k} + 2w)^2 \sigma^2 + i\phi}] \right) \right.
\end{aligned} \tag{2.30}$$

Here under the time-reversal relation, $u_k^*(\vec{r}) = u_{-k}(\vec{r})$, so for $-k$, we have:

$$\left\langle \frac{\partial u_{v,-k}}{\partial(-k)} \left| u_{c,-k} \right\rangle \frac{\partial \left\langle u_{c,-k} \left| \frac{\partial u_{v,-k}}{\partial(-k)} \right\rangle}{\partial(-k)} = \left\langle \frac{\partial u_{v,k}^*}{\partial(-k)} \left| u_{c,k}^* \right\rangle \frac{\partial \left\langle u_{c,k}^* \left| \frac{\partial u_{v,k}}{\partial(-k)} \right\rangle}{\partial(-k)} \tag{2.31}$$

$$= - \left\langle u_{c,k} \left| \frac{\partial u_{v,k}}{\partial k} \right\rangle \frac{\partial \left\langle \frac{\partial u_{v,k}}{\partial k} \left| u_{c,k} \right\rangle}{\partial k} \tag{2.32}$$

The interference terms for central symmetry point $-k$ can be written as:

$$\begin{aligned}
c_{c,-k}^{(1)}(t)^* c_{c,-k,dip}^{(2)}(t) + c.c. &= \frac{\sqrt{2} A_1 A_2^2 \vec{e} w^2 \cdot \sigma^2 \pi}{4} \cdot (e^{-\frac{\sigma^2}{4} (\Delta \epsilon_{vc,k} - 2w)^2} - e^{-\frac{\sigma^2}{4} (\Delta \epsilon_{vc,k} + 2w)^2}) \\
&\cdot \left(- \left\langle u_{c,k} \left| \frac{\partial u_{v,k}}{\partial k} \right\rangle \frac{\partial \left\langle \frac{\partial u_{v,k}}{\partial k} \left| u_{c,k} \right\rangle}{\partial k} [e^{-\frac{1}{2} (\Delta \epsilon_{vc,k} - 2w)^2 \sigma^2 + i\phi} - e^{-\frac{1}{2} (\Delta \epsilon_{vc,k} + 2w)^2 \sigma^2 - i\phi}] \right. \right. \\
&\left. \left. - \frac{\partial \left\langle u_{c,k} \left| \frac{\partial u_{v,k}}{\partial k} \right\rangle}{\partial k} \left\langle \frac{\partial u_{v,k}}{\partial k} \left| u_{c,k} \right\rangle [e^{-\frac{1}{2} (\Delta \epsilon_{vc,k} - 2w)^2 \sigma^2 - i\phi} - e^{-\frac{1}{2} (\Delta \epsilon_{vc,k} + 2w)^2 \sigma^2 + i\phi}] \right) \right.
\end{aligned} \tag{2.33}$$

$$\begin{aligned}
 c_{c,k,dyn}^{(2)}(t)^* c_{c,k,dip}^{(2)}(t) + c.c. &= \frac{(A_2 \vec{e})^4 w \cdot \sigma^2 \pi}{8} \cdot [e^{-\frac{\sigma^2}{4}(\Delta\epsilon_{vc,k}-2w)^2} - e^{-\frac{\sigma^2}{4}(\Delta\epsilon_{vc,k}+2w)^2}] \\
 &\cdot [e^{-\frac{\sigma^2}{4}\Delta\epsilon_{vc,k}^2} - \frac{1}{2}(e^{-\frac{\sigma^2}{4}(\Delta\epsilon_{vc,k}-2w)^2} + e^{-\frac{\sigma^2}{4}(\Delta\epsilon_{vc,k}+2w)^2})] \\
 &\cdot \frac{\partial \Delta\epsilon_{vc,k}}{\partial k} \left(\left\langle \frac{\partial u_{v,k}}{\partial k} \middle| u_{c,k} \right\rangle \frac{\partial \left\langle u_{c,k} \middle| \frac{\partial u_{v,k}}{\partial k} \right\rangle}{\partial k} + \frac{\partial \left\langle \frac{\partial u_{v,k}}{\partial k} \middle| u_{c,k} \right\rangle}{\partial k} \left\langle u_{c,k} \middle| \frac{\partial u_{v,k}}{\partial k} \right\rangle \right)
 \end{aligned} \tag{2.34}$$

$$\begin{aligned}
 c_{c,-k,dyn}^{(2)}(t)^* c_{c,-k,dip}^{(2)}(t) + c.c. &= \frac{(A_2 \vec{e})^4 w \cdot \sigma^2 \pi}{8} \cdot [e^{-\frac{\sigma^2}{4}(\Delta\epsilon_{vc,k}-2w)^2} - e^{-\frac{\sigma^2}{4}(\Delta\epsilon_{vc,k}+2w)^2}] \\
 &\cdot [e^{-\frac{\sigma^2}{4}\Delta\epsilon_{vc,k}^2} - \frac{1}{2}(e^{-\frac{\sigma^2}{4}(\Delta\epsilon_{vc,k}-2w)^2} + e^{-\frac{\sigma^2}{4}(\Delta\epsilon_{vc,k}+2w)^2})] \\
 &\cdot \frac{\partial \Delta\epsilon_{vc,k}}{\partial k} \left(\left\langle u_{c,k} \middle| \frac{\partial u_{v,k}}{\partial k} \right\rangle \frac{\partial \left\langle \frac{\partial u_{v,k}}{\partial k} \middle| u_{c,k} \right\rangle}{\partial k} + \frac{\partial \left\langle u_{c,k} \middle| \frac{\partial u_{v,k}}{\partial k} \right\rangle}{\partial k} \left\langle \frac{\partial u_{v,k}}{\partial k} \middle| u_{c,k} \right\rangle \right) \\
 &= c_{c,k,dyn}^{(2)}(t)^* c_{c,k,dip}^{(2)}(t) + c.c.
 \end{aligned} \tag{2.35}$$

To summarize the steps, the asymmetric population distribution between k and $-k$ can be understood by the quantum interference (Qul) of different excitation paths:

2.1. TIME-DEPENDENT PERTURBATIVE ANALYSIS ON QUI

$$\begin{aligned}
|c_{c,k}(t)|^2 - |c_{c,-k}(t)|^2 &= 2c_{c,k}^{(1)}(t)^* c_{c,k,dyn}^{(2)}(t) + c_{c,k}^{(1)}(t)^* c_{c,k,dip}^{(2)}(t) - c_{c,-k}^{(1)}(t)^* c_{c,-k,dip}^{(2)}(t) + c.c. \\
&= 2\sqrt{2}A_1 A_2^2 \vec{e} w \cdot \sigma^2 \pi \frac{\partial \Delta \epsilon_{vc,k}}{\partial k} \left| \left\langle u_{c,k} \left| \frac{\partial u_{v,k}}{\partial k} \right\rangle \right|^2 \right. \\
&\quad \cdot [e^{-\frac{\sigma^2}{4} \Delta \epsilon_{vc,k}^2} - \frac{1}{2}(e^{-\frac{\sigma^2}{4} (\Delta \epsilon_{vc,k} - 2w)^2} + e^{-\frac{\sigma^2}{4} (\Delta \epsilon_{vc,k} + 2w)^2})] \\
&\quad \cdot [e^{-\frac{1}{2} (\Delta \epsilon_{vc,k} - 2w)^2 \sigma^2} - e^{-\frac{1}{2} (\Delta \epsilon_{vc,k} + 2w)^2 \sigma^2}] \cos \phi \\
&\quad + \frac{\sqrt{2}A_1 A_2^2 \vec{e} w^2 \cdot \sigma^2 \pi}{2} \cdot (e^{-\frac{\sigma^2}{4} (\Delta \epsilon_{vc,k} - 2w)^2} - e^{-\frac{\sigma^2}{4} (\Delta \epsilon_{vc,k} + 2w)^2}) \\
&\quad \cdot \left(\left\langle u_{c,k} \left| \frac{\partial u_{v,k}}{\partial k} \right\rangle \frac{\partial \left\langle \frac{\partial u_{v,k}}{\partial k} \right| u_{c,k} \right\rangle}{\partial k} + \frac{\partial \left\langle u_{c,k} \left| \frac{\partial u_{v,k}}{\partial k} \right\rangle}{\partial k} \left\langle \frac{\partial u_{v,k}}{\partial k} \right| u_{c,k} \right\rangle \right) \\
&\quad \cdot [e^{-\frac{1}{2} (\Delta \epsilon_{vc,k} - 2w)^2 \sigma^2} - e^{-\frac{1}{2} (\Delta \epsilon_{vc,k} + 2w)^2 \sigma^2}] \cos \phi \\
&= \sqrt{2}A_1 A_2^2 \vec{e} w \cdot \sigma^2 \pi [e^{-\frac{1}{2} (\Delta \epsilon_{vc,k} - 2w)^2 \sigma^2} - e^{-\frac{1}{2} (\Delta \epsilon_{vc,k} + 2w)^2 \sigma^2}] \\
&\quad \cdot \left[\frac{\partial \Delta \epsilon_{vc,k}}{\partial k} \left| \left\langle u_{c,k} \left| \frac{\partial u_{v,k}}{\partial k} \right\rangle \right|^2 (2e^{-\frac{\sigma^2}{4} \Delta \epsilon_{vc,k}^2} - e^{-\frac{\sigma^2}{4} (\Delta \epsilon_{vc,k} - 2w)^2} - e^{-\frac{\sigma^2}{4} (\Delta \epsilon_{vc,k} + 2w)^2}) \right. \right. \\
&\quad \left. \left. + \frac{w}{2} \left(\left\langle u_{c,k} \left| \frac{\partial u_{v,k}}{\partial k} \right\rangle \frac{\partial \left\langle \frac{\partial u_{v,k}}{\partial k} \right| u_{c,k} \right\rangle}{\partial k} + \frac{\partial \left\langle u_{c,k} \left| \frac{\partial u_{v,k}}{\partial k} \right\rangle}{\partial k} \left\langle \frac{\partial u_{v,k}}{\partial k} \right| u_{c,k} \right\rangle \right) \right. \\
&\quad \left. \cdot (e^{-\frac{1}{4} (\Delta \epsilon_{vc,k} - 2w)^2 \sigma^2} - e^{-\frac{1}{4} (\Delta \epsilon_{vc,k} + 2w)^2 \sigma^2}) \right] \cos \phi
\end{aligned} \tag{2.36}$$

We consider the band gap between valence and conduction bands close to twice the field's frequency:

$$\Delta \epsilon_{vc,k} + 2w \approx 0 \tag{2.37}$$

Because $\sigma \gg 0$. In a nutshell, the population imbalance becomes:

$$\begin{aligned}
|c_{c,k}(t)|^2 - |c_{c,-k}(t)|^2 &\approx \sqrt{2}A_1 A_2^2 \vec{e} w \cdot \sigma^2 \pi e^{-\frac{3}{4} (\Delta \epsilon_{vc,k} + 2w)^2 \sigma^2} \left[\frac{\partial \Delta \epsilon_{vc,k}}{\partial k} \left| \left\langle u_{c,k} \left| \frac{\partial u_{v,k}}{\partial k} \right\rangle \right|^2 \right. \right. \\
&\quad \left. \left. + \frac{w}{2} \left(\left\langle u_{c,k} \left| \frac{\partial u_{v,k}}{\partial k} \right\rangle \frac{\partial \left\langle \frac{\partial u_{v,k}}{\partial k} \right| u_{c,k} \right\rangle}{\partial k} + \frac{\partial \left\langle u_{c,k} \left| \frac{\partial u_{v,k}}{\partial k} \right\rangle}{\partial k} \left\langle \frac{\partial u_{v,k}}{\partial k} \right| u_{c,k} \right\rangle \right) \right] \cos \phi
\end{aligned} \tag{2.38}$$

The utilization of two-color fields, such as ω and 2ω , has opened a potential to break the time-reversal symmetry of the systems, even when the combined field is linearly polarized. This symmetry breaking leads to a population imbalance

induced by laser irradiation, consequently resulting in dc-current injection. The population imbalance in this scheme is caused by quantum interference between two excitation paths: One is the two-photon absorption process with photons at the frequency ω , while the other is the one-photon absorption process with photons at the frequency 2ω . Hence, this protocol for dc-current injection is known as quantum interference control (QuIC). By manipulating the relative phase of the optical fields at frequencies ω and 2ω , QuIC can be applied to achieve control over one- and two-photon absorption processes, often referred to as $(1 + 2 \text{ QuIC})$.

2.2 Third-order Nonlinear Regime: $1 + 2 \text{ QuIC}$

From perturbation analysis in Sec 2.1, the disruption of time-reversal symmetry can be achieved through the use of linearly polarized light featuring two distinct frequencies. This implies that the injection of dc-current and the generation of a substantial population imbalance can be efficiently realized without relying on the ellipticity of light. This principle is exemplified by employing two-color linearly polarized laser fields with frequencies ω and 2ω . In this configuration, the intrinsic properties of linear polarization and the dual frequencies are sufficient to break time-reversal symmetry, facilitating the desired outcomes of dc-current injection and the establishment of a pronounced population imbalance. This approach provides a versatile and simplified means to manipulate quantum interference and achieve specific optical responses in the system without the need for elliptically polarized light. This protocol for dc-current injection is also known as quantum interference control (QuIC). By manipulating the relative phase of the optical fields at frequencies ω and 2ω , QuIC can be applied to achieve control over one- and two-photon absorption processes, often referred to as $(1 + 2 \text{ QuIC})$.

For practical simulation, we examine the light-induced electron dynamics in a prototypical two-dimensional insulator, monolayer hexagonal boron-nitride (*h*-BN), using a simple tight-binding approximation and TDSEs introduced in Chapter 1. In the quantum dynamics simulation, we employ the following expression for the vector potential of the applied two-color fields within the interval

$-\frac{\tau}{2} < t < \frac{\tau}{2}$ and zero outside this range:

$$A(t) = -e_p \frac{E_0}{\omega} \left[\cos(\omega t) + \frac{1}{4} \cos(2\omega t + \phi) \right] \times \cos^4\left(\frac{\pi}{\tau} t\right)$$

e_p represents a unit vector along the polarization direction of the laser field, E_0 denotes the peak field strength, ω is the fundamental frequency, and τ is the duration of the laser field pulse. To illustrate dc current injection according to perturbation derivation in Section 2.1, we simulate electron dynamics using the vector potential from Eq. (2.40) with ω set to 3 eV for practical calculations. Note that the photon energy satisfies the condition ($\omega \leq E_g \leq 2\hbar\omega$) for the 1+2 QuIC process [14]. Furthermore, we set the laser polarization direction, e_p , with the Γ - K direction, the pulse duration, τ , is set to 40 fs. We introduce a relative phase ϕ between the two-color fields. The relative phase governs quantum interferences among different excitation paths induced via ω and 2ω laser fields, while the global phase is utilized to extract a dc-like response from the quantum dynamics. By manipulating the relative phase ϕ in the electric field described in Eq. (2.39):

$$E(t) = -e_p E_0 \left[\cos(\omega t) + \frac{1}{2} \cos(2\omega t + \phi) \right]$$

one can induce a population imbalance and, consequently, a dc-current by extrinsically breaking the time-reversal symmetry by utilizing two-color fields with frequencies ω and 2ω . Figure 2.1 (a) illustrates the electric field generated by the vector potential with a relative phase of $\phi = 0$, while Figure 2.1 (b) presents the field with a relative phase of $\phi = \pi/2$. It is evident that the field with $\phi = 0$ in Fig. 2.1 (a) breaks the time-reversal symmetry, as $E(t) \neq E(-t)$, while the field with $\phi = \pi/2$ in Fig. 2.1 (b) maintains the symmetry $E(t) = E(-t)$. Hence, the time-reversal symmetry of the Hamiltonian is broken when $\phi = 0$ and preserved when $\phi = \pi/2$. Consequently, a population imbalance and resulting dc current injection are expected when $\phi = 0$, while symmetric excitation population and the absence of net residual current are anticipated when $\phi = \pi/2$.

To comprehensively assess the persistent dc-current following laser irradiation, we conduct an in-depth analysis utilizing the photo-excited conduction population n_{ck} computed from Eq. (1.26). Employing a weak enough laser field in the perturbation region with a strength of $E_0 = 2.57$ MV/cm and fixing the relative

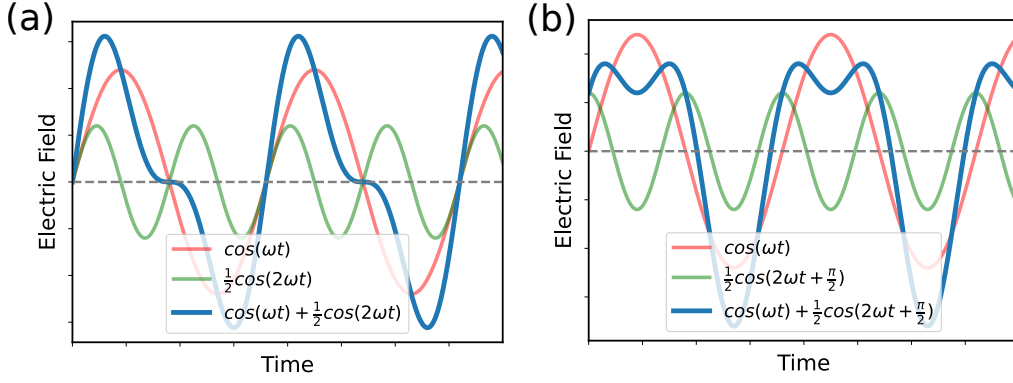


Figure 2.1: The time profiles of the electric field given by Eq. (2.39) are shown for (a) $\phi = 0$ and (b) $\phi = \pi/2$.

phase at $\phi = 0$, the resulting conduction population is illustrated in Fig. 2.2 (a). For comparative purposes, Fig. 2.2 (b) presents the conduction population n_{ck} computed under the same field strength ($E_0 = 2.57$ MV/cm) but with a distinct relative phase ($\phi = 0$). In both instances, the conduction populations exhibit notable excitations centered around the K - and K' -points. This observation implies that the photo-absorption process is primarily governed by a one-photon absorption at the photon energy of $2\hbar\omega$ and a two-photon absorption at the photon energy of $\hbar\omega$. The consistency in the excitation patterns further underscores the dominance of these absorption mechanisms in the system under the specified laser conditions.

While the population distributions in Fig. 2.2(a) and (b) may initially appear similar, a closer examination reveals nuanced distinctions. In the scenario of the time-reversal symmetry-broken field ($\phi = 0$) illustrated in Fig. 2.2(a), the population distribution must manifest an imbalance between time-reversal Kramers pairs (e.g., k and $-k$, or K and K'). On the contrary, in the case of the time-reversal field ($\phi = \pi/2$) showcased in Fig. 2.2(b), the population distribution n_{ck} is anticipated to lack such a population imbalance. This discrepancy arises from the absence of a persistent current under these conditions. This nuanced analysis deepens our understanding of the intricate relationship between population distributions and the underlying time-reversal symmetry characteristics, providing crucial insights into the dynamic behavior of the system.

To delineate the population imbalance across the Brillouin zone, we introduce the population imbalance distribution $\Delta n_{c\vec{k}}$, defined as the disparity in popula-

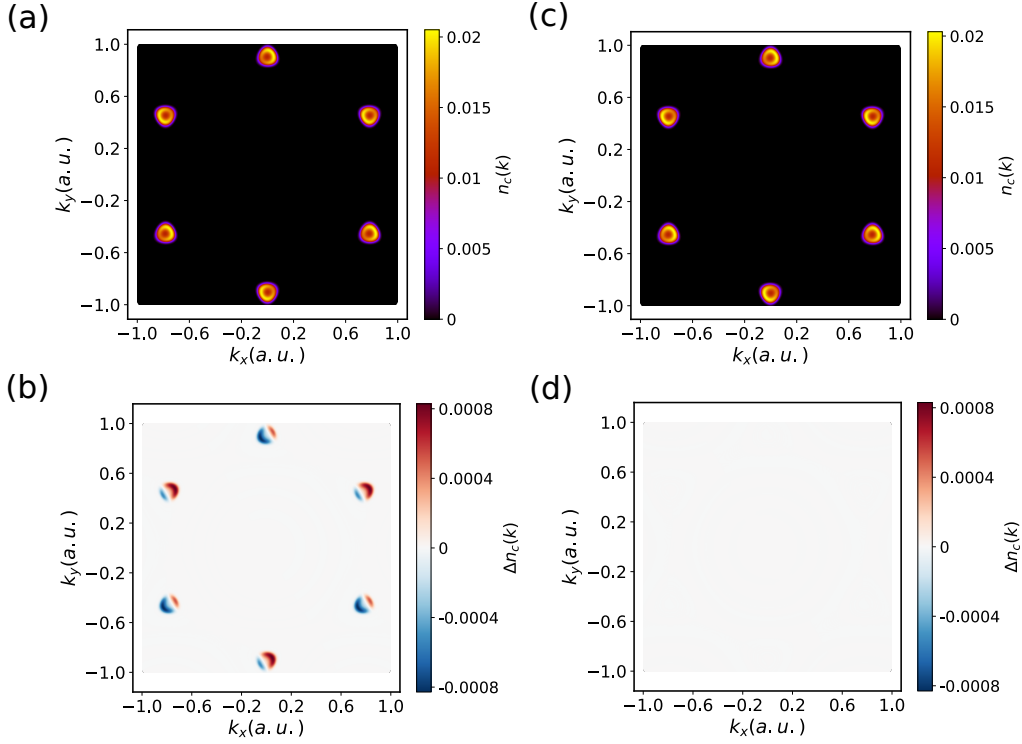


Figure 2.2: (a, b) The conduction population distribution $n_c(k)$ computed with (a) $\phi = 0$ and (b) $\phi = \pi/2$. (c, d) The population imbalance distribution $\Delta n_c(k)$ computed with (c) $\phi = 0$ and (d) $\phi = \pi/2$.

tion between the time-reversal pair k -points, expressed as:

$$\Delta n_{ck} = n_{ck} - n_{c,-k} \quad (2.39)$$

Given the constraint $0 \leq n_{ck} \leq 1$, the population imbalance distribution is bounded by $-1 \leq \Delta n_{ck} \leq 1$. In scenarios where external fields maintain time-reversal symmetry, the populations at k and $-k$ are equivalent, resulting in a population imbalance distribution of zero. Conversely, in instances where time-reversal symmetry is broken, non-equivalent populations can be induced at k and $-k$, giving rise to a finite population imbalance distribution Δn_{ck} . Figures 2.2(c) and (d) depict the population imbalance distribution, Δn_{ck} , derived from the population distributions presented in Figs. 2.2 (a) and (b), respectively. The figures clearly illustrate that when the external field disrupts time-reversal symmetry ($\phi = 0$), a discernible finite population imbalance is induced. In contrast, when the field preserves time-reversal symmetry ($\phi = \pi/2$), the population imbalance diminishes entirely. This comprehensive analysis of the population imbalance distri-

bution provides a detailed insight into the intricate interplay between external field characteristics and the resulting population asymmetry within the Brillouin zone.

The temporal evolution of the corresponding electric current, denoted as $J_{total}(t)$, can be computed using Eq.(1.20). This equation represents a functional dependence on the vector potential $A(t)$, as depicted in Fig.2.3. The total current encompasses multiple components and noises, often overshadowing the relatively small value of the dc-component following the laser pulse. To pragmatically examine and isolate the dc-current generated by the fields, we introduce the global phase θ into the fields as described by the Eq.(2.40), as done in our prior study[21].

$$A(t) = -e_p \frac{E_0}{\omega} \left[\cos(\omega t + \theta) + \frac{1}{4} \cos(2\omega t + 2\theta + \phi) \right] \times \cos^4\left(\frac{\pi}{\tau} t\right)$$

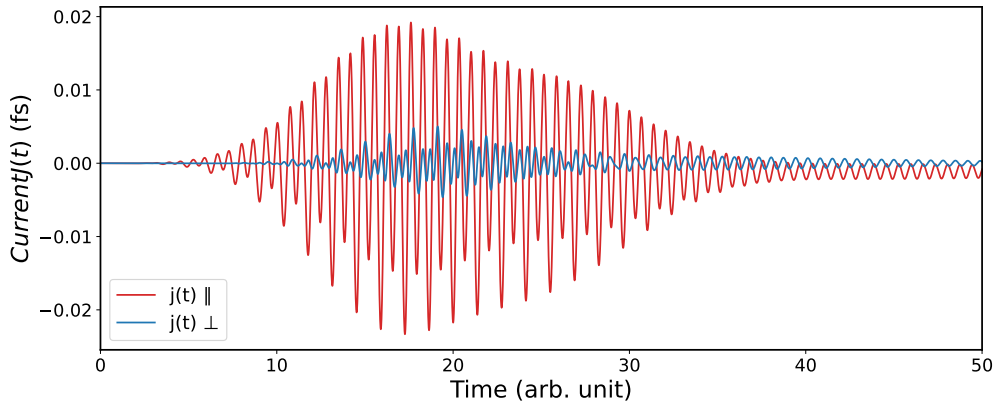


Figure 2.3

The time profiles of the current computed from Eq. (1.20) induced by the electric field given by Eq. (2.39) as shown in Fig. 2.1(a) with relative phase $\phi = 0$.

The current, expressed as a function of the global phase θ in accordance with the vector potential given by Eq.(2.40), is explicitly denoted as $J(t, \theta)$. By maintaining all laser parameters constant in Eq.(2.40) except for the global phase θ , we can isolate the direct current (dc)-like component of the induced current through the following integral:

$$J_{dc}(t) = \frac{1}{2\pi} \int_0^{2\pi} d\theta, J(t, \theta). \quad (2.40)$$

In this formulation, the integral averages out the higher-frequency components, enabling the extraction of the clean dc-like slow-frequency component of the induced current.

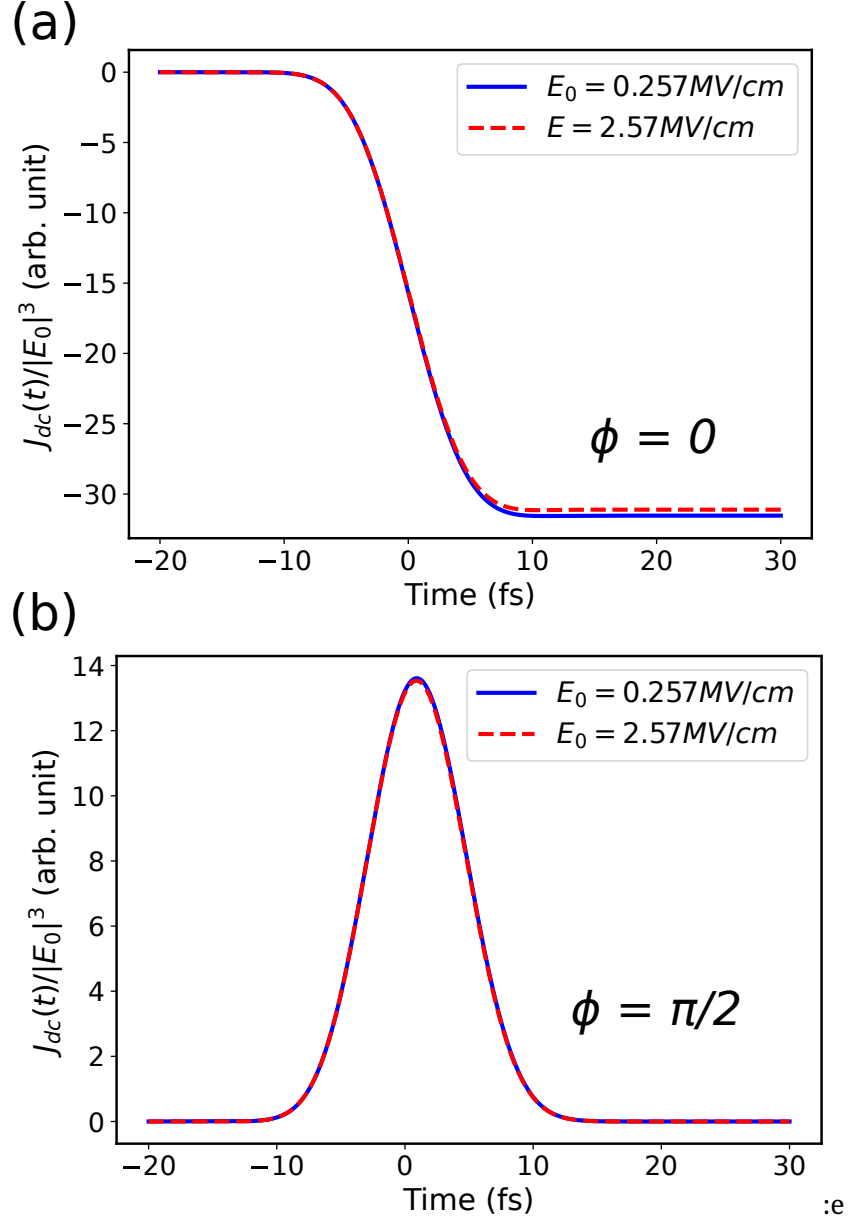


Figure 2.4: The dc components of the currents $J_{dc}(t)$ computed from Eq. (2.40) are shown as a function of time. The results using the relative phase of $\phi = 0$ are shown in panel (a), while those using $\phi = \pi/2$ are shown in (b)

In Figure 2.4(a), the calculated direct current (dc) component of the scaled current, $J_{\text{dc}}(t)/E_0^3$, is presented for a relative phase of $\phi = 0$, encompassing results for various field strengths, E_0 . Remarkably, the residual dc-current persists beyond the conclusion of the laser fields ($t > \tau/2$). Notably, the scaled quantity, $J_{\text{dc}}(t)/E_0^3$, maintains identical behavior across different field strengths. This consistency suggests that the dc component of the induced current can be interpreted as a third-order nonlinear optical effect. This interpretation aligns with the inherent nature of the 1+2 QuIC process, which involves interference between one- and two-photon absorption processes, categorizing it as a third-order nonlinear optical phenomenon. The presented results shed light on the robust and field-independent nature of the observed third-order nonlinear optical effects in the system.

In Figure 2.4(b), the dc-current component of the scaled current, $J_{\text{dc}}(t)/E_0^3$, is depicted with a relative phase of $\phi = \pi/2$. In stark contrast to the results with $\phi = 0$ shown in Fig. 2.4(a), the currents in Fig. 2.4 (b) do not manifest a persistent dc component after the conclusion of the laser irradiation. This outcome signifies that the applied field with a relative phase of $\phi = \pi/2$ does not disrupt time-reversal symmetry, and consequently, no population imbalance is induced, resulting in the absence of a sustained current. It is noteworthy that, even in the case of $\phi = \pi/2$, the dc-component of the current is induced solely during the laser irradiation, highlighting yet another instance of a third-order nonlinear optical process. This observation provides further insight into the nuanced interplay between field characteristics and the resulting dynamical responses in the system.

By manipulating the relative phase ϕ , one gains control over the extent of time-reversal symmetry breaking, thereby influencing the resulting population imbalance and dc- current injection [13]. For subsequent analysis, we systematically explore the persistent dc current by varying the relative phase ϕ . Figure 2.5 illustrates the dependence of the dc-current on the relative phase ϕ after laser irradiation, computed using a field with a strength of $E_0 = 2.57$ MV/cm. The amplitude of the induced dc current reaches its maximum when $\phi = 0$ and $\phi = \pi$, with opposite signs for these two phases. Moreover, the induced dc current exhibits continuous variation as the phase ϕ is manipulated, attaining zero when $\phi = \pi/2$

and $\phi = 3\pi/2$, corresponding to the points where the applied fields restore time-reversal symmetry. This straightforward phase dependence aligns with findings from prior works[13, 15], providing further validation of the controllable nature of the induced dc current through manipulation of the relative phase.

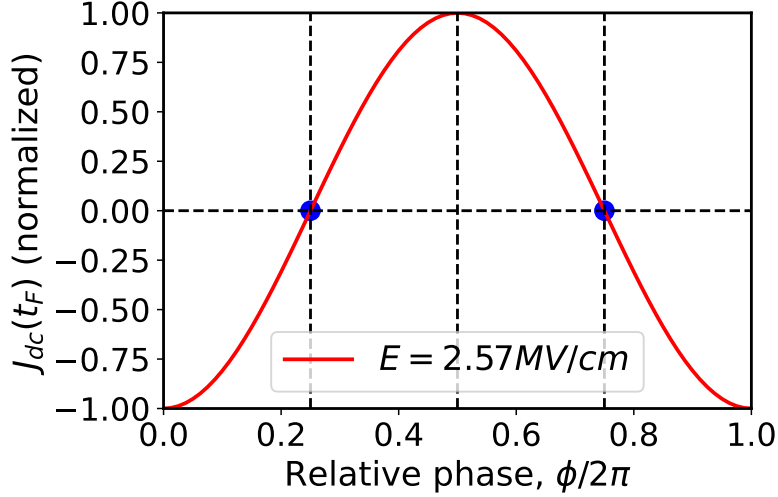


Figure 2.5: The persistent current $J_{dc}(t_f)$ as a function of the relative phase, ϕ . The results are computed by setting E_0 to 2.57 MV/cm and $\hbar\omega$ to 3 eV.

QuIC processes often exhibit resonance conditions at specific photon energies. By systematically investigating the photon-energy dependence, we can identify resonant regions where the interference effects are significantly enhanced. Investigating these dependencies aids in identifying the primary mechanisms at play. To scrutinize this phenomenon within our theoretical framework, we systematically evaluate the direct current (dc) after laser irradiation by varying the fundamental frequency ω in Eq.(2.40). Figure 2.6 (a) illustrates the resulting dc current following laser irradiation with a field strength of $E_0 = 1.03$ MV/m.

In line with the anticipated behavior of the 1 + 2 QuIC process, the residual dc-current diminishes when the fundamental photon energy falls below half of the band gap, i.e., $\hbar\omega \leq E_g/2 = 2.95$ eV, since the fundamental photon energy $\hbar\omega$ must adhere to the condition $\hbar\omega \geq E_g/2$, where E_g signifies the band gap. In instances where the fundamental photon energy $\hbar\omega$ falls below the gap, both the 1 + 2 QuIC process and the resultant direct current (dc) vanish. This exploration not only elucidates the pivotal role of photon energy in the manifestation of the 1 + 2 QuIC process but also underscores the significance of satisfying specific conditions for

its occurrence and subsequent dc-current induction. This behavior aligns with the expected characteristics of the $1 + 2$ QuIC process and provides valuable insights into the influence of the fundamental frequency on the induced dc-current in our theoretical framework.

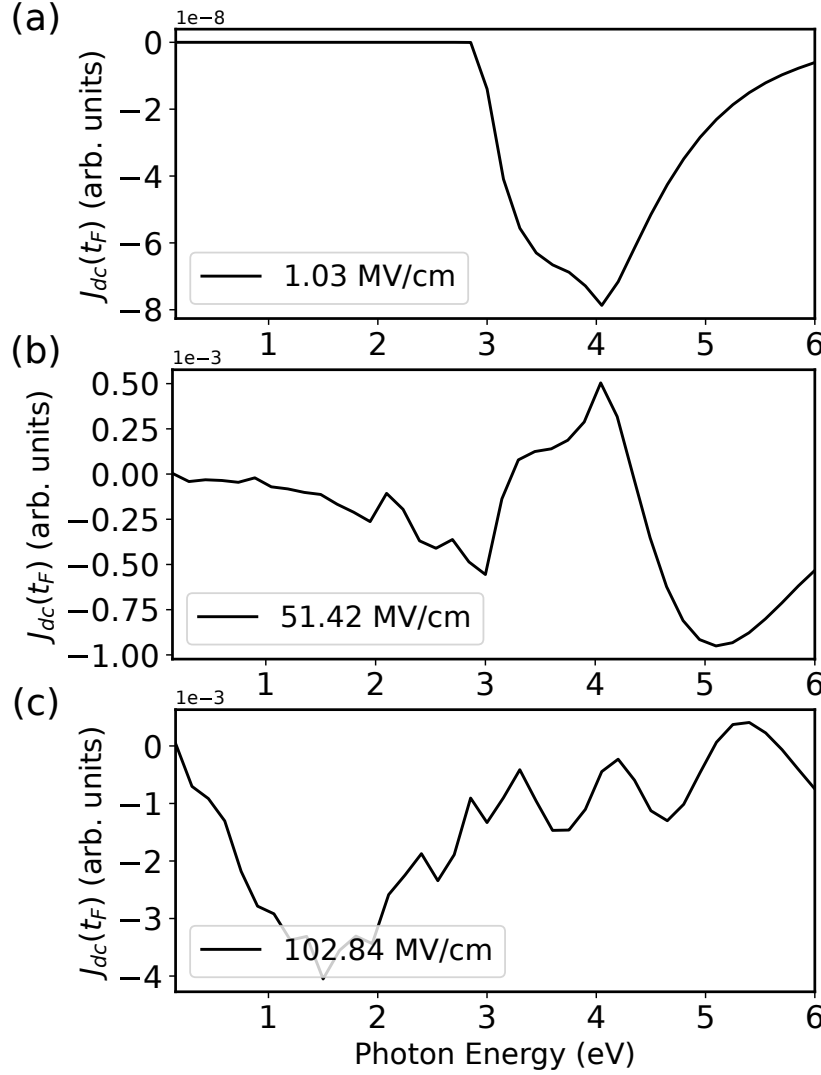


Figure 2.6: The current after the laser irradiation is shown as a function of the fundamental photon energy $\hbar\omega$. The results computed different field strengths: (a) $E_0 = 1.03$ MV/cm, (b) 51.43 MV/cm, and (c) $E_0 = 102.84$ MV/cm.

The investigation aids in comprehending the intricate relationship between photon energy, field strength, and the ensuing nonlinear processes. It is imperative to investigate the photon energy dependence of the direct current (dc) after laser irradiation while systematically varying the field strength, E_0 , to unravel the intricacies of this highly nonlinear optical phenomenon. Figures 2.6 (b)

and (c) meticulously depict the photon-energy dependence of the persistent current following laser irradiation, calculated for two distinct field strengths: (b) $E_0 = 51.42$ MV/cm and (c) $E_0 = 102.84$ MV/cm. In stark contrast to the weak field regime typified by the 1 + 2 QuIC, the direct current (dc) can be induced even under deeply off-resonant conditions, where the photon energy is smaller than half of the band gap ($\hbar\omega \leq E_g/2$), as evident in Figure 2.6(b). This compelling observation suggests that potent laser fields introduce additional pathways for electron excitation that extend beyond the realm of two-photon absorption. These additional processes, involving multiple photons, contribute to the creation of a population imbalance and a residual dc current, even in the deeply off-resonant regime. The nuanced interplay between laser field strength and photon energy unveiled in these results provides invaluable insights into the complex dynamics governing persistent currents in strong-field regimes.

Illustrated in Figure 2.6 (c), a noteworthy observation emerges the magnitude of the direct current (dc) after laser irradiation in the deeply off-resonant regime ($\hbar\omega \leq E_g/2$) surpasses that in the 1 + 2 QuIC regime ($\hbar\omega \geq E_g/2$) as the applied field strength reaches exceptionally large values. This intriguing behavior finds its explanation in the ponderomotive energy, denoted as:

$$U_p = \frac{e^2 E_0^2}{4m\pi\omega_0^2} \quad (2.41)$$

The associated light-induced intraband transitions, both of which are more substantial for lower frequency driving[22]. Consequently, the ensuing nonlinear effects and the injection of dc current become more pronounced in the deeply off-resonant regime compared to the resonant condition. Our initial investigation focused on analyzing the electric current induced by these two-color laser fields within the weak field regime. We confirmed that the dc-component of the induced current persists even after laser irradiation when the fundamental photon energy $\hbar\omega$ exceeds the optical gap, $E_g/2$. This ballistic current phenomenon originates from a population imbalance in the Brillouin zone, arising from quantum interference between two distinct excitation paths: one involving one-photon absorption at the photon energy of $2\hbar\omega$, and the other involving a two-photon absorption path at the photon energy of $\hbar\omega$ [13–15].

This discovery sets the stage for a more in-depth exploration in the subsequent section, where we will delve into the intricacies of efficiently inducing DC current through highly nonlinear optical processes in the deeply off-resonant regime.

2.3 Deeply off-resonant highly-nonlinear regime

Despite the significant interest in the nonlinear photovoltaic effect, there has been limited exploration of efficient current injection in the deeply off-resonant regime with multi-cycle light pulses, particularly using linearly polarized light. Subsequently, the scope of QuIC can be broadened to involve general integer combinations, denoted as $M + N$ QuIC [17, 19]. In this extended scheme, two-color laser fields operating at frequencies ω and ω' induce M - and N -photon absorption processes, respectively. To investigate the mechanism of dc-current injection in the deeply off-resonant regime, as demonstrated in the previous section, we fix the fundamental photon energy $\hbar\omega$ in Eq. (2.40) at 1 eV. Notably, this value is much smaller than half of the band gap, $E_g/2 = 2.95$ eV, for this section.

Similarly, we start with evaluating the population imbalance induced by a strong field in the deeply off-resonant regime, we calculate the population distribution $n_{c\vec{k}}$ after irradiating the laser field with a strength of 100 MV/cm. A distinct pattern emerges in the excited carrier population distribution around the K and K' points. This pattern can be understood through the multi-photon absorption resonances of the light-induced Floquet states[23]. In Fig.2.7(a), we present the computed population distribution in the conduction band. As anticipated from the preceding discussion, the photo-carrier distribution reveals a significant population imbalance between k and $-k$ points. To enhance clarity in visualizing the population imbalance, we compute the population imbalance distribution $\Delta n_{ck} = n_{ck} - n_{c,-k}$. Figure 2.7(b) displays the resulting population imbalance distribution Δn_{ck} . Since Δn_{ck} is constrained by $-1 \leq \Delta n_{ck} \leq 1$, the population imbalance between k and $-k$ is maximized when $|\Delta n_{ck}| = 1$. As observed in Fig.2.7 (b), the population imbalance distribution takes significantly large values, comparable to the maximum values (± 1), across a wide range of the Brillouin zone.

We calculate the population imbalance ratio r_{im} defined as the maximum absolute value of the population imbalance distribution Δn_{ck} across the Brillouin zone for further qualification. Mathematically, it is expressed as:

$$r_{im} = \frac{\int_{BZ} dk |\Delta n_{ck}|}{\int_{BZ} dk (n_{ck} + n_{c,-k})} = \frac{\int_{BZ} dk |\Delta n_{ck}|}{2 \int_{BZ} dk n_{ck}}. \quad (2.42)$$

The computed imbalance ratio, r_{im} , from Figs. 2.7(a) and (b) is about 0.307. Hence, more than 30% of the excited electrons contribute to the population imbalance. This implies the potential for realizing a significant population imbalance through the use of linearly polarized light alone.

In an earlier study [20], significant control over valley population was proposed using bi-circular fields with counter-rotating ω and 2ω two-color laser fields. In contrast, in this work, we demonstrate that significant valley population can be induced without relying on circular or elliptically polarized light; rather, bi-color linearly polarized light alone can break the time-reversal symmetry and cause such population control.

We commence our analysis of population imbalance by examining the light-induced current in the time domain within the deeply off-resonant regime. In Figure 2.8, we present the dc component of the current, $J_{dc}(t)/E_0^3$, computed with varying field strengths, E_0 . For this analysis, the relative phase ϕ is set to 0. Evidently, a third-order nonlinear response dominates the induced current in the case of weak field strength. Given that the photon energy of the second harmonic is smaller than the band-gap ($2\hbar\omega < E_g$) and the QuIC process is forbidden, the third-order current returns to zero after the laser irradiation.

However, as the field strength becomes sufficiently strong, the dc-component remains finite even after laser irradiation, as depicted in Fig. 2.8. This observation suggests that a higher-order nonlinear process contributes to the ballistic dc-current injection beyond the third-order nonlinear effect.

Next, we explore the dependence of the ballistic current induced by deeply off-resonant light on the relative phase, ϕ . Figure 2.9 illustrates the computed current as a function of the relative phase, ϕ , with calculations conducted at a field strength of $E_0 = 2 \times 10 \text{ MV/cm}$. In accordance with the QuIC case shown in

Fig.2.5, the persistent current is maximized when the relative phase is $\phi = 0$ or $\phi = \pi$, and it vanishes when the applied field exhibits time-reversal symmetry ($\phi = \pi/2$ or $\phi = 3\pi/2$). Therefore, even in the deeply off-resonant regime, the direction and magnitude of the persistent current can be controlled by manipulating the relative phase ϕ between the two-color fields at frequencies ω and 2ω .

To gain a more detailed understanding of the intricate mechanism behind dc current injection in the deeply off-resonant regime, we delve into an analysis of how the injected current scales with the applied field strength E_0 . As depicted in Figure 2.10, the current amplitude after laser irradiation is plotted against the varying field strength. Notably, a reference line representing $|E_0|^7$ is included for comparison.

The compelling observation from the figure is that the induced current exhibits a clear proportionality to $|E_0|^7$ in the weak field regime. This insightful finding suggests that the seventh-order nonlinear process takes precedence in governing the dynamics of dc current injection under these conditions. This nuanced understanding provides a comprehensive insight into the intricate nonlinear optical processes that contribute to the observed dc current phenomena in the deeply off-resonant regime.

The observed scaling law of the induced dc current with the applied field strength might initially seem inconsistent with the expected behavior of a straightforward $M + N$ QuIC process. In the conventional $M + N$ QuIC scenario, the M -photon absorption process is initiated by light with frequency ω , and the N -photon absorption process is triggered by light with frequency 2ω , resulting in an overall $(M + N)$ -th order nonlinear process. For instance, if we consider a six-photon process for multi-photon absorption with light of frequency ω and a three-photon process for light of frequency 2ω , the anticipated simple $M + N$ QuIC process corresponds to the ninth-order nonlinear process ($M + N = 6 + 3 = 9$).

However, our experimental observations reveal a scaling that indicates seventh-order nonlinearity instead. This apparent discrepancy in the observed and expected nonlinearities of the injected dc current can be rationalized by the presence of an additional excitation channel involving a four-photon absorption process. In this scenario, two photons at frequency ω and the other two photons

at frequency 2ω combine to excite electrons. This additional four-photon excitation channel interferes with the three-photon absorption process at the photon energy of $2\hbar\omega$, resulting in seventh-order ($7 = 3 + 4$) nonlinear current injection.

To delve deeper into the nonlinearity of the light-induced electron dynamics, we performed computations to determine the number of photo-excited carriers after laser irradiation using the expression:

$$N_{ex} = \frac{2}{A_{\text{BZ}}} \int_{\text{BZ}} dk n_{c,k}, \quad (2.43)$$

where $A_{\text{BZ}} = \int_{\text{BZ}} dk$ represents the area of the Brillouin zone.

Figure 2.10 (b) presents the number of excited electrons as a function of the field strength, E_0 , alongside a reference line proportional to $|E_0|^6$. In the weak field regime, the number of excited electrons exhibits proportionality to $|E_0|^6$, highlighting the dominance of the three-photon absorption process in the excitation mechanism. However, as the field strength increases, the deviation from the three-photon absorption line suggests the initiation of a nonperturbative mechanism in the excitation process.

In contrast to the $|E_0|^6$ -dependence of the number of photo-excited carriers in the weak field regime, the injected current and the corresponding population imbalance follow a $|E_0|^7$ scaling, as depicted in Figure 2.10 (a). The difference in nonlinearities between the absolute photo-carrier population and the population imbalance implies that the population imbalance is negligible concerning the absolute photo-carrier population in the weak field regime. However, in a strong field regime, the relative significance of the population imbalance becomes substantial as it grows more rapidly than the absolute photo-carrier population. Therefore, the distinction in nonlinearities between the total photocarrier population and the population imbalance indicates the potential for large-amplitude valley carrier population control.

Expanding our analysis to the deeply off-resonant regime, where $\hbar\omega \ll E_g/2$, we observed an absence of population imbalance under weak applied field strength. However, as the field strength increased, a population imbalance in the Brillouin zone is formed, leading to the injection of the persistent dc-current after the laser

irradiation. Scaling analysis of the ballistic current injection with respect to the applied field strength E_0 revealed that the population imbalance and the ballistic current result from an interference between three-photon absorption process with three photons of energy $2\hbar\omega$ and a four-photon absorption process with two photons of energy $2\hbar\omega$ and two photons of energy $\hbar\omega$. Consequently, we demonstrated that a multi-photon absorption process, incorporating photons with different energies, plays a pivotal role in addition to the multi-photon absorption process involving single-color photons.

In previous works [20, 24, 25], the formation of substantial population imbalance and valley-population control has been discussed in monolayer systems such as monolayer *h*-BN and graphene, using bi-circular laser fields with frequencies ω and 2ω . Recently, valley-population control with bi-circular fields has been extended to multi-layer and bulk systems [26] without relying on intrinsic inversion symmetry breaking and the Berry curvature at the valleys. In contrast to these works, our study demonstrates the induction of a large population imbalance and ballistic current injection without relying on the ellipticity of light. Instead, we rely on time-reversal symmetry breaking achieved through relative phase control between two-color linearly-polarized fields at frequencies ω and 2ω . Furthermore, similar to Ref. [26], the injection mechanism with bi-color linearly polarized light does not rely on intrinsic inversion symmetry breaking, indicating an efficient dc current injection and population control with the scheme using linearly-polarized light. The potential of population control and the photovoltaic effect with linearly polarized light, in addition to circularly/elliptically polarized light, unveils novel avenues for realizing ultrafast opto-electronics, marked by precise control of current and population dynamics on the femtosecond time scale.

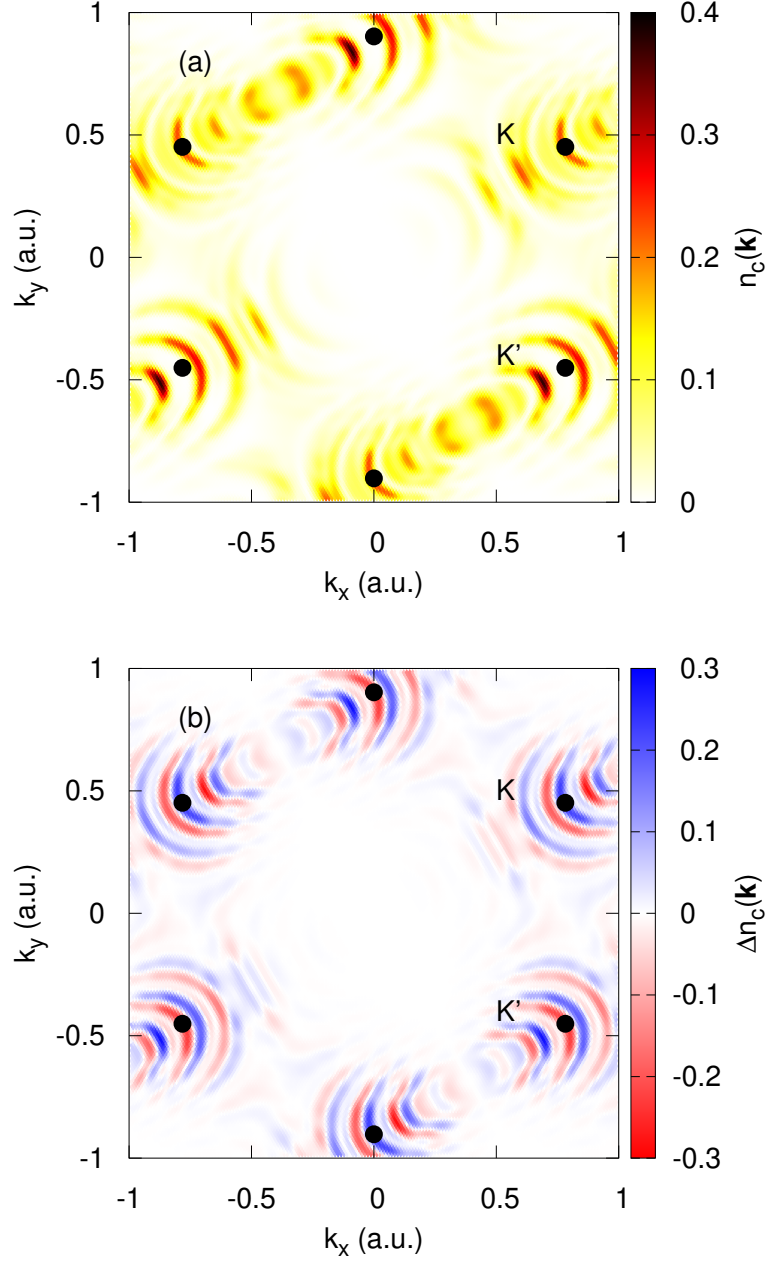


Figure 2.7: (a) The conduction population distribution $n_c(k)$ after the irradiation of the laser field, and (b) the population imbalance distribution $\Delta n_c(k)$ are shown. The results are computed by setting E_0 to 10^{10} V/m.

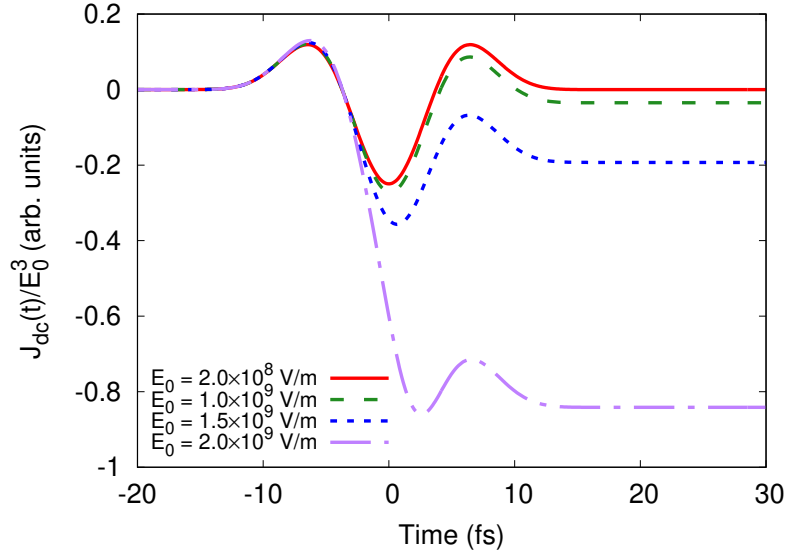


Figure 2.8: The dc components of the currents, $J_{dc}(t)$, are shown as a function of time. The results are computed with the deeply off-resonant condition, $\hbar\omega = 1.0$ eV.

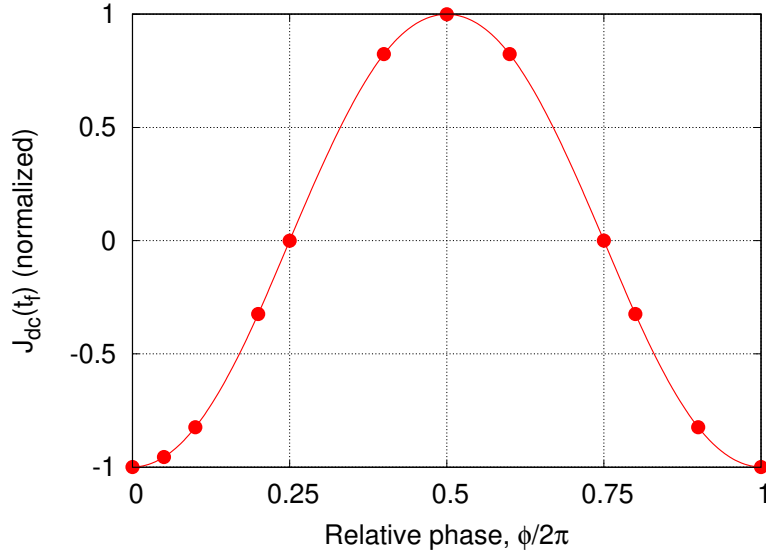


Figure 2.9: The persistent current, $J_{dc}(t_f)$, is shown as a function of the relative phase ϕ . The results are computed with the deeply off-resonant condition, $\hbar\omega = 1.0$ eV.

2.3. DEEPLY OFF-RESONANT HIGHLY-NONLINEAR REGIME

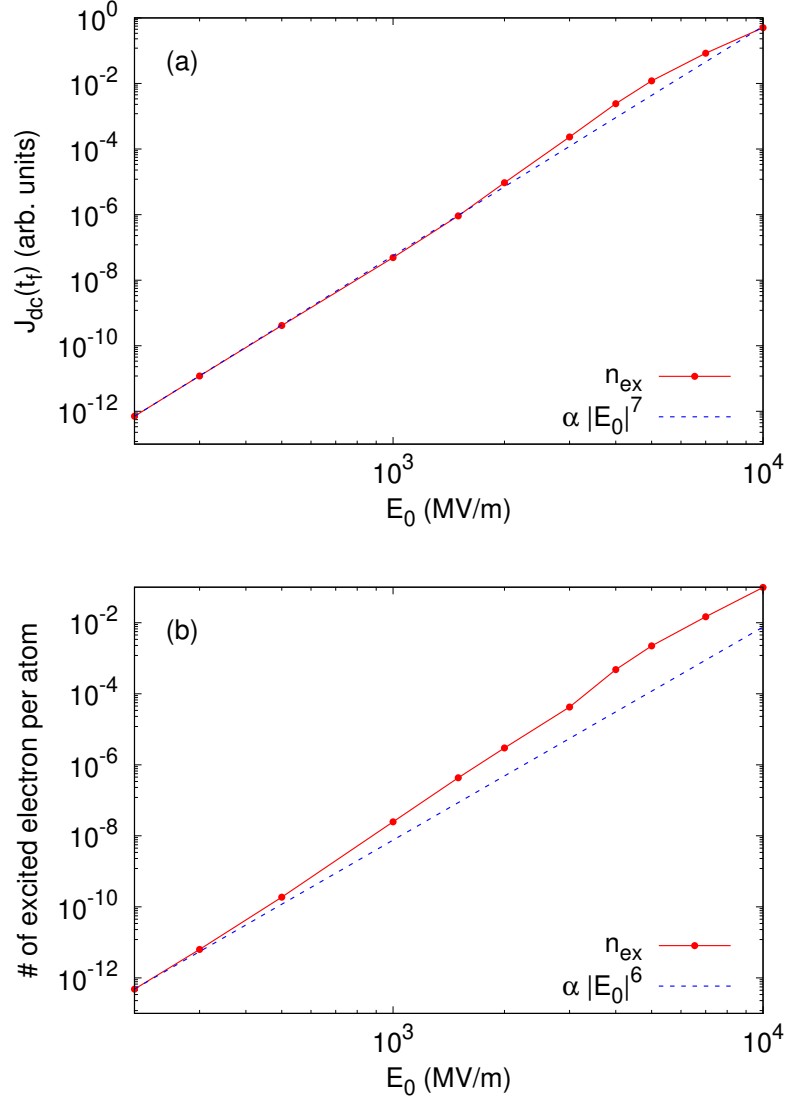


Figure 2.10: (a) The persistent current, $|J_{dc}(t_f)|$, is shown as a function of the field strength, E_0 . (b) The number of conduction population after the laser irradiation is shown as a function of the field strength E_0 .

This page is intentionally left blank.

ADIABATIC BASIS REPRESENTATION

To analytically investigate nonlinear photocarrier injection in solids, we first introduce the equation of motion in the adiabatic basis representation. In this representation, we can naturally separate the interband transitions, the dynamical phase factor, and the geometric phase factor. To introduce the representation, we consider the following one-body Schrödinger equation for a k -point,

$$i \frac{d}{dt} |\psi_k(t)\rangle = H[k + A(t)] |\psi_k(t)\rangle, \quad (\text{A.1})$$

where $A(t)$ is an external vector potential, which is related to the external electric field as $E(t) = -dA(t)/dt$. In this note, we assume that the vector potential is zero for the negative time; $A(t \leq 0) = 0$.

To introduce the adiabatic basis representation, we introduce the instantaneous eigenstates of the Hamiltonian as

$$H[k + A(t)] |u_{b,k+A(t)}\rangle = \epsilon_{b,k+A(t)} |u_{b,k+A(t)}\rangle, \quad (\text{A.2})$$

where b is the band index. Hereafter, we assume the two-band system, which has the valence band ($b = v$) and the conduction band ($b = c$). However, we can straightforwardly extend it to general systems.

On the basis of the instantaneous eigenstates defined by Eq. (A.2), we consider

APPENDIX A. ADIABATIC BASIS REPRESENTATION

the following expansion of the wavefunction

$$|\psi_k(t)\rangle = c_{v,k}(t)e^{-i\int_0^t dt' \epsilon_{v,k+A(t')}} e^{i\phi_{v,k}^g(t)} |u_{v,k+A(t)}\rangle + c_{c,k}(t)e^{-i\int_0^t dt' \epsilon_{c,k+A(t')}} e^{i\phi_{c,k}^g(t)} |u_{c,k+A(t)}\rangle, \quad (\text{A.3})$$

where $c_{b,k}(t)$ are the expansion coefficients. In the expansion, we explicitly include the dynamical phase factor, $e^{-i\int_0^t dt' \epsilon_{v,k+A(t')}}$, and the additional phase factor, $e^{i\phi_{b,k}^g(t)}$. The latter one will be defined later as the geometric phase factor.

Inserting Eq. (A.3) into Eq. (??), one obtains

$$\begin{aligned} \left[i \frac{d}{dt} - H[k + A(t)] \right] |\psi_k(t)\rangle = & i\dot{c}_{v,k}(t)e^{-i\int_0^t dt' \epsilon_{v,k+A(t')}} e^{i\phi_{v,k}^g(t)} |u_{v,k+A(t)}\rangle \\ & + i\dot{c}_{c,k}(t)e^{-i\int_0^t dt' \epsilon_{c,k+A(t')}} e^{i\phi_{c,k}^g(t)} |u_{c,k+A(t)}\rangle \\ & - \dot{\phi}_{v,k}^g(t)c_{v,k}(t)e^{-i\int_0^t dt' \epsilon_{v,k+A(t')}} e^{i\phi_{v,k}^g(t)} |u_{v,k+A(t)}\rangle \\ & - \dot{\phi}_{c,k}^g(t)c_{c,k}(t)e^{-i\int_0^t dt' \epsilon_{c,k+A(t')}} e^{i\phi_{c,k}^g(t)} |u_{c,k+A(t)}\rangle \\ & - ic_{v,k}(t)e^{-i\int_0^t dt' \epsilon_{v,k+A(t')}} e^{i\phi_{v,k}^g(t)} E(t) \cdot \frac{\partial |u_{v,k+A(t)}\rangle}{\partial k} \\ & - ic_{c,k}(t)e^{-i\int_0^t dt' \epsilon_{c,k+A(t')}} e^{i\phi_{c,k}^g(t)} E(t) \cdot \frac{\partial |u_{c,k+A(t)}\rangle}{\partial k} = 0. \end{aligned} \quad (\text{A.4})$$

By multiplying $e^{+i\int_0^t dt' \epsilon_{v,k+A(t')}} e^{-i\phi_{v,k}^g(t)} \langle u_{v,k+A(t)} |$ to Eq. (A.4), one obtains

$$\begin{aligned} i\dot{c}_{v,k}(t) - \dot{\phi}_{v,k}^g(t)c_{v,k}(t) - ic_{v,k}(t)E(t) \cdot \left\langle u_{v,k+A(t)} \left| \frac{\partial u_{v,k+A(t)}}{\partial k} \right\rangle \right. \\ \left. - ic_{c,k}(t)e^{-i\int_0^t dt' \epsilon_{c,k+A(t')} - \epsilon_{v,k+A(t')}} e^{i(\phi_{c,k}^g(t) - \phi_{v,k}^g(t))} E(t) \cdot \left\langle u_{v,k+A(t)} \left| \frac{\partial u_{c,k+A(t)}}{\partial k} \right\rangle \right\rangle = 0. \end{aligned} \quad (\text{A.5})$$

Likewise, by multiplying $e^{+i\int_0^t dt' \epsilon_{c,k+A(t')}} e^{-i\phi_{c,k}^g(t)} \langle u_{c,k+A(t)} |$ to Eq. (A.4), one obtains

$$\begin{aligned} i\dot{c}_{c,k}(t) - \dot{\phi}_{c,k}^g(t)c_{c,k}(t) - ic_{c,k}(t)E(t) \cdot \left\langle u_{c,k+A(t)} \left| \frac{\partial u_{c,k+A(t)}}{\partial k} \right\rangle \right. \\ \left. - ic_{v,k}(t)e^{-i\int_0^t dt' \epsilon_{v,k+A(t')} - \epsilon_{c,k+A(t')}} e^{i(\phi_{v,k}^g(t) - \phi_{c,k}^g(t))} E(t) \cdot \left\langle u_{c,k+A(t)} \left| \frac{\partial u_{v,k+A(t)}}{\partial k} \right\rangle \right\rangle = 0. \end{aligned} \quad (\text{A.6})$$

Combining Eq. (A.5) and Eq. (A.6), one can obtain the following matrix form,

$$\begin{aligned}
i \frac{d}{dt} c_k(t) &= \begin{pmatrix} \dot{\phi}_{v,k}^g(t) & 0 \\ 0 & \dot{\phi}_{c,k}^g(t) \end{pmatrix} c_k(t) \\
&+ iE(t) \cdot \begin{pmatrix} \left\langle u_{v,k+A(t)} \left| \frac{\partial u_{v,k+A(t)}}{\partial k} \right\rangle & e^{-i \int_0^t dt' \Delta \epsilon_{cv,k+A(t')} + i \Delta \phi_{cv,k}^g(t)} \left\langle u_{v,k+A(t)} \left| \frac{\partial u_{c,k+A(t)}}{\partial k} \right\rangle \\ e^{-i \int_0^t dt' \Delta \epsilon_{vc,k+A(t')} + i \Delta \phi_{vc,k}^g(t)} \left\langle u_{c,k+A(t)} \left| \frac{\partial u_{v,k+A(t)}}{\partial k} \right\rangle & \left\langle u_{v,k+A(t)} \left| \frac{\partial u_{v,k+A(t)}}{\partial k} \right\rangle \end{pmatrix} c_k(t)
\end{aligned} \tag{A.7}$$

where $\Delta \epsilon_{bb',k+A(t)}$ is defined by the difference of the single particle energies as $\epsilon_{b,k+A(t)} - \epsilon_{b',k+A(t)}$, and $\Delta \phi_{bb',k}^g(t)$ is defined by the difference of the geometric phases as $\phi_{b,k}^g(t) - \phi_{b',k}^g(t)$. Here, the coefficient vector was introduced as

$$c_k(t) = \begin{pmatrix} c_{v,k}(t) \\ c_{c,k}(t) \end{pmatrix}. \tag{A.8}$$

Here, we define the geometric phases as

$$\begin{aligned}
\phi_{b,k}^g(t) &= -i \int_0^t dt' E(t') \cdot \left\langle u_{b,k+A(t')} \left| \frac{\partial u_{b,k+A(t')}}{\partial k} \right\rangle = i \int_0^t dt' \frac{dA(t')}{dt'} \cdot \left\langle u_{b,k+A(t')} \left| \frac{\partial u_{b,k+A(t')}}{\partial k} \right\rangle \\
&= i \oint_{A(0)}^{A(t)} dA \cdot \left\langle u_{b,k+A} \left| \frac{\partial u_{b,k+A}}{\partial k} \right\rangle.
\end{aligned} \tag{A.9}$$

As seen from the last expression in Eq. (A.9), the phase $\phi_{b,k}^g$ depends only on the geometry of the path of the integral.

With the expression of the geometric phases in Eq. (A.9), one can rewrite the equation of motion for the coefficient vector as

$$\begin{aligned}
i \frac{d}{dt} c_k(t) &= \\
iE(t) \cdot \begin{pmatrix} 0 & e^{-i \int_0^t dt' \Delta \epsilon_{cv,k+A(t')} + i \Delta \phi_{cv,k}^g(t)} \left\langle u_{v,k+A(t)} \left| \frac{\partial u_{c,k+A(t)}}{\partial k} \right\rangle \\ e^{-i \int_0^t dt' \Delta \epsilon_{vc,k+A(t')} + i \Delta \phi_{vc,k}^g(t)} \left\langle u_{c,k+A(t)} \left| \frac{\partial u_{v,k+A(t)}}{\partial k} \right\rangle & 0 \end{pmatrix} c_k(t) \\
&= \mathcal{H}(t) c_k(t).
\end{aligned} \tag{A.10}$$

This is nothing but the time-dependent Schrödinger equation on the adiabatic basis, and it is closely related to the Houston basis expansion [10, 11].

This page is intentionally left blank.

Bibliography

1. Sarma, S. D., Adam, S., Hwang, E. & Rossi, E. Electronic transport in two-dimensional graphene. *Reviews of modern physics* **83**, 407 (2011).
2. Sławińska, J., Zasada, I. & Klusek, Z. Energy gap tuning in graphene on hexagonal boron nitride bilayer system. *Phys. Rev. B* **81**, 155433. <https://link.aps.org/doi/10.1103/PhysRevB.81.155433> (15 Apr. 2010).
3. Blase, X., Rubio, A., Louie, S. G. & Cohen, M. L. Quasiparticle band structure of bulk hexagonal boron nitride and related systems. *Phys. Rev. B* **51**, 6868–6875. <https://link.aps.org/doi/10.1103/PhysRevB.51.6868> (11 Mar. 1995).
4. Hofstadter, D. R. Energy levels and wave functions of Bloch electrons in rational and irrational magnetic fields. *Phys. Rev. B* **14**, 2239–2249. <https://link.aps.org/doi/10.1103/PhysRevB.14.2239> (6 Sept. 1976).
5. Sato, S. A. *et al.* Light-induced anomalous Hall effect in massless Dirac fermion systems and topological insulators with dissipation. *New Journal of Physics* **21**, 093005. <https://doi.org/10.1088/1367-2630/ab3acf> (Sept. 2019).
6. Sato, S. A. *et al.* Microscopic theory for the light-induced anomalous Hall effect in graphene. *Phys. Rev. B* **99**, 214302. <https://link.aps.org/doi/10.1103/PhysRevB.99.214302> (21 June 2019).
7. Sato, S. A., Hirori, H., Sanari, Y., Kanemitsu, Y. & Rubio, A. High-order harmonic generation in graphene: Nonlinear coupling of intraband and interband transitions. *Phys. Rev. B* **103**, L041408. <https://link.aps.org/doi/10.1103/PhysRevB.103.L041408> (4 Jan. 2021).
8. Sato, S. A. & Rubio, A. Nonlinear electric conductivity and THz-induced charge transport in graphene. *New Journal of Physics* **23**, 063047. <https://doi.org/10.1088/1367-2630/ac03d0> (June 2021).
9. Meier, T., von Plessen, G., Thomas, P. & Koch, S. W. Coherent Electric-Field Effects in Semiconductors. *Phys. Rev. Lett.* **73**, 902–905. <https://link.aps.org/doi/10.1103/PhysRevLett.73.902> (6 Aug. 1994).

BIBLIOGRAPHY

10. Houston, W. V. Acceleration of Electrons in a Crystal Lattice. *Phys. Rev.* **57**, 184–186. <https://link.aps.org/doi/10.1103/PhysRev.57.184> (3 Feb. 1940).
11. Krieger, J. B. & Iafrate, G. J. Time evolution of Bloch electrons in a homogeneous electric field. *Phys. Rev. B* **33**, 5494–5500. <https://link.aps.org/doi/10.1103/PhysRevB.33.5494> (8 Apr. 1986).
12. Sato, S. A. *et al.* Microscopic theory for the light-induced anomalous Hall effect in graphene. *Phys. Rev. B* **99**, 214302. <https://link.aps.org/doi/10.1103/PhysRevB.99.214302> (21 June 2019).
13. Dupont, E., Corkum, P. B., Liu, H. C., Buchanan, M. & Wasilewski, Z. R. Phase-Controlled Currents in Semiconductors. *Phys. Rev. Lett.* **74**, 3596–3599. <https://link.aps.org/doi/10.1103/PhysRevLett.74.3596> (18 May 1995).
14. Atanasov, R., Haché, A., Hughes, J. L. P., van Driel, H. M. & Sipe, J. E. Coherent Control of Photocurrent Generation in Bulk Semiconductors. *Phys. Rev. Lett.* **76**, 1703–1706. <https://link.aps.org/doi/10.1103/PhysRevLett.76.1703> (10 Mar. 1996).
15. Haché, A. *et al.* Observation of Coherently Controlled Photocurrent in Unbiased, Bulk GaAs. *Phys. Rev. Lett.* **78**, 306–309. <https://link.aps.org/doi/10.1103/PhysRevLett.78.306> (2 Jan. 1997).
16. Sun, D. *et al.* Coherent Control of Ballistic Photocurrents in Multilayer Epitaxial Graphene Using Quantum Interference. *Nano Letters* **10**, 1293–1296. ISSN: 1530-6984. <https://doi.org/10.1021/nl9040737> (Apr. 2010).
17. Muniz, R. A., Salazar, C., Wang, K., Cundiff, S. T. & Sipe, J. E. Quantum interference control of carriers and currents in zinc blende semiconductors based on nonlinear absorption processes. *Phys. Rev. B* **100**, 075202. <https://link.aps.org/doi/10.1103/PhysRevB.100.075202> (7 Aug. 2019).
18. Heide, C., Boolakee, T., Eckstein, T. & Hommelhoff, P. *Nanophotonics* **10**, 3701–3707. <https://doi.org/10.1515/nanoph-2021-0236> (2021).
19. Wang, K., Muniz, R. A., Sipe, J. E. & Cundiff, S. T. Quantum Interference Control of Photocurrents in Semiconductors by Nonlinear Optical Absorption Processes. *Phys. Rev. Lett.* **123**, 067402. <https://link.aps.org/doi/10.1103/PhysRevLett.123.067402> (6 Aug. 2019).
20. Jiménez-Galán, Á., Silva, R. E. F., Smirnova, O. & Ivanov, M. Lightwave control of topological properties in 2D materials for sub-cycle and non-resonant valley manipulation. *Nature Photonics* **14**, 728–732. ISSN: 1749-4893. <https://doi.org/10.1038/s41566-020-00717-3> (Dec. 2020).
21. Sato, S. A. & Rubio, A. *Limitations of mean-field approximations in describing shift-current and injection-current in materials* 2023. arXiv: 2310.08875 [cond-mat.mtrl-sci].
22. Sato, S. A. *et al.* Role of intraband transitions in photocarrier generation. *Phys. Rev. B* **98**, 035202. <https://link.aps.org/doi/10.1103/PhysRevB.98.035202> (3 July 2018).

23. Galler, A., Rubio, A. & Neufeld, O. *Mapping light-dressed Floquet bands by highly nonlinear optical excitations and valley polarization* 2023. arXiv: 2303.15055 [physics.optics].
24. Mrudul, M. S., Jiménez-Galán, Á., Ivanov, M. & Dixit, G. Light-induced valleytronics in pristine graphene. *Optica* **8**, 422–427. <https://opg.optica.org/optica/abstract.cfm?URI=optica-8-3-422> (Mar. 2021).
25. Neufeld, O., Tancogne-Dejean, N., De Giovannini, U., Hübener, H. & Rubio, A. Light-Driven Extremely Nonlinear Bulk Photogalvanic Currents. *Phys. Rev. Lett.* **127**, 126601. <https://link.aps.org/doi/10.1103/PhysRevLett.127.126601> (12 Sept. 2021).
26. Tyulnev, I. *et al.* *Valleytronics in bulk MoS₂ by optical control of parity and time symmetries* 2023. arXiv: 2302.12564 [cond-mat.mtrl-sci].